International Journal of Heat and Mass Transfer 258 (2026) 128297

Contents lists available at ScienceDirect

International Journal of Heat and Mass Transfer

journal homepage: www.elsevier.com/locate/ijhmt

Adjoint inversion-informed machine learning for optimizing turbulent Prandtl number in supercritical flows: A case study of hydrogen fuel flows under cross conditions

Feng Sun [a,*], Bo Zhang [a], Jinkun Yan [a], Gongnan Xie [c], Jinliang Xu [a,b]

[a] Beijing Key Laboratory of Multiphase Flow and Heat Transfer for Low Grade Energy Utilization, North China Electric Power University, Beijing, 102206, PR China
[b] Key Laboratory of Power Station Energy Transfer Conversion and System, North China Electric Power University, Ministry of Education, Beijing 102206, China
[c] School of Marine Science and Technology, Northwestern Polytechnical University, Xi'an, 710072, China

ARTICLE INFO

Keywords:
Supercritical fluids
Turbulence model
Turbulent Prandtl number
Adjoint inversion
machine learning

ABSTRACT

Developing accurate turbulence models for supercritical flows is challenging due to the flawed assumption that the turbulent Prandtl number (Pr_t) is constant and typically set to 0.85. This paper proposes an adjoint-based inversion method to optimize the full-spatial Pr_t by computing temperature gradient differences between RANS and LES data. Firstly, the inversion method, implemented in the SU2 solver, calculated temperature discrepancies across 10^8 grid points. Secondly, the principal flow features were identified using Pearson correlation analysis as inputs of a new hybrid neural network based on radial basis function (RBF) and multi-layer perceptron (MLP) methods, namely RBF-MLP. This network was designed to achieve precise nonlinear approximation to align RANS results from the inverted Pr_t model with LES data. Finally, the hydrocarbon fuel flows were used to train and test the new Pr_t model across various channels and flow directions. The constant-Pr_t model showed significant deviations from LES data, particularly near walls, while the adjoint-based Pr_t model closely matched LES trends. In rectangular channels, the adjoint-based model had a maximum error of 2% under 0.189 MW/m^2 and 5% under 0.341 MW/m^2. In circular channels, prediction errors rose with heat flux, but the adjoint-based Pr_t model's maximum error was only 4%, compared to 20% of the conventional model. In vertical channels, the adjoint-based Pr_t model maintained an error within 4.2%, while the constant-Pr_t model had a 14.29% error. Across all test cases, the adjoint-based model demonstrated superior accuracy, reducing the mean absolute relative error (e_R) to 1.1–12.5% and the root mean-square relative error (e_S) to 1.3–16.4%, compared to the conventional model's e_R=5.8–68.7% and e_S=8.3–68.7%. In summary, this adjoint-based inversion offers significant advantages in developing turbulence models by capturing nonlinear, complex relationships from large datasets. It also extends universality to diverse flow cases, and supports reliable turbulence modeling for supercritical flows.

1. Introduction

Supercritical fluids (SCFs) feature high specific heat capacity, low viscosity, strong thermal diffusivity. These properties have driven their wide adoption in advanced energy and power systems [1]. Examples include thermal protection for aerospace engines, supercritical Brayton cycle power generation, renewable energy systems, nuclear reactor propulsion, and carbon capture and storage facilities [2,3]. It highlights their significant value in clean energy and propulsion technologies. However, unlocking the full thermal efficiency potential of SCF-based systems requires a mechanistic understanding of SCF flow and heat transfer in channels [4]. Notably, SCFs exhibit distinct nonlinear thermophysical property variations, causing complex phenomena such as abrupt density change, buoyancy effect, and flow acceleration. Hence, the accurate characterization and analysis of SCFs' flow and heat transfer behaviors are essential for achieving high thermal efficiency in energy and propulsion technologies.

Over recent decades, extensive experiments have been conducted to study the flow and heat transfer characteristics of SCFs [5,6]. However, the high-temperature and high-pressure operating conditions impose constraints. Most experimental measurements are limited to the external wall temperature, as well as inlet/outlet velocities and pressures. Such data support analyzing wall heat transfer mechanisms and developing

* Corresponding author.
E-mail address: fengsun@ncepu.edu.cn (F. Sun).

https://doi.org/10.1016/j.ijheatmasstransfer.2025.128297
Received 27 September 2025; Received in revised form 8 December 2025; Accepted 19 December 2025
Available online 26 December 2025
0017-9310/© 2025 Elsevier Ltd. All rights are reserved, including those for text and data mining, AI training, and similar technologies.

Nomenclature

Bo^*	Modified buoyancy number
Bu	Buoyancy parameter
c_p	Specific heat capacity, J/(kg·K)
C_w	WALE model constant
d	Diameter, m
e_i	Relative error
e_R	Mean absolute relative error
e_S	Root mean-square relative *error*
$\widetilde{E}$	Total energy, kJ/kg
Ea	Activation energy, kJ/mol
G	Mass flux, kg/(m^2·s)
Gr	Grashof *number*
Gr_b^*	Modified bulk Grashof number
h	Heat transfer coefficient, W/(m^2·K)
$\widetilde{H}$	Total enthalpy, kJ/*kg*
J	Objective *function*
k	Turbulent kinetic energy, m^2/s^2
k_0	Pre-exponential factor, s^{-1}
K	Rate constant, s^{-1}
l	Characteristic length, m
Nu	Nusselt number
P	Pressure, Pa
P_b	Buoyancy production term, m^2/s^3
Pr	Prandtl number
Pr_t	Turbulent Prandtl number
P_s	Shear production term, m^2/s^3
q	Heat flux, W/m^2
q_b^+	Normalized bulk heat flux
$\overline{q}_j$	Molecular heat flux, W/m^2
R	Regression coefficients
Re	Reynolds number
T	Temperature, K
u	Velocity, m/s
$\widetilde{S}_{ij}$	Favre-averaged strain rate tensor, s^{-1}

Greek symbols

α_t	Turbulent thermal diffusivity, m^2/s
β	Volumetric coefficient, 1/K
λ	Thermal conductivity, W/m·K
μ	Dynamic viscosity, Pa·s
μ_t	Turbulent eddy viscosity, Pa·s
ν_t	Turbulent kinematic viscosity, m^2/s
ρ	Density, kg/m^3
$\overline{\tau}_{ij}$	Molecular viscous stress tensor, N/m^2
ω_R	Reaction rate, mol/(m^3·s)

Subscripts

b	Bulk fluid condition
in	Inlet condition
ref	Reference data
sgs	Subgrid-scale
w	Wall *condition*

Abbreviation

AHFM	Algebraic Heat Flux Model
CFD	Computational Fluid *Dynamics*
DNS	Direct Numerical *Simulation*
GGDH	Generalized Gradient *Diffusion* Hypothesis
HTD	Heat Transfer *Deterioration*
LES	Large Eddy *Simulation*
ML	Machine Learning
MLP	Multilayer Perceptron
PDE	Partial *Differential* Equation
RANS	Reynolds-*Averaged* Navier-Stokes
RBF	Radial Basis *Function*
SCF	Supercritical fluid
SGDH	Simple Gradient *Diffusion* Hypothesis
SST	Shear Stress *Transport*
SU2	Stanford *University* Unstructured

empirical correlations for thermal design [7,8], but offer limited insights into internal turbulent transport mechanisms. In contrast, numerical simulations serve as a valuable complement to experimental method. It provides detailed descriptions of supercritical flow and thermal transport characteristics. Numerical methods generally include direct numerical simulation (DNS), large eddy simulation (LES), and Reynolds-averaged Navier-Stokes (RANS) modeling. DNS and LES offer high accuracy but incur prohibitively high computational costs. Thus, RANS remains dominant in current and foreseeable large-scale simulations for supercritical industrial applications [9]. Nevertheless, compared to high-fidelity data from LES or DNS, RANS can exhibit predictive errors in excess of 10 % under extreme conditions, like near the pseudo-critical point where buoyancy and flow acceleration effects are notable [4].

Conventional turbulence models assuming constant thermophysical properties fail to accurately simulate supercritical flow characteristics [10,11]. A potential limitation stems from the isotropic eddy viscosity hypothesis of RANS turbulence equations. These models treat turbulence as an equivalent viscous effect governing both momentum transfer and energy transport. By contrast, supercritical flows near the pseudo-critical point exhibit severe density gradients, e.g.,$\partial\rho\ /\partial T$ up to 100-fold. It gives rise to significant buoyancy effect ($Gr \propto g\beta\Delta T l^3\ /\nu^2$) and thermal acceleration effect ($\frac{du}{dx} \propto -\frac{1}{T}\frac{dT}{dx}$). The complex flow phenomena described above lead to significant modifications in the turbulent transport processes. It is particularly evident in mechanisms such as the redistribution of turbulent kinetic energy in the near-wall region. However, conventional eddy viscosity models, being inherently isotropic, struggle to fully represent these complex flow dynamics and their consequent impact on the Reynolds stresses, especially the normal stress components.

For thermal performance, the sharp peak in specific heat capacity (c_p) within the pseudo-critical region significantly alters the thermal boundary layer. Hence, the conventional Reynolds analogy fails in such conditions. In thermal engineering, some practitioners prioritize thermal aspects over flow structure. Within RANS models, turbulent heat flux is defined as,

$$-\overline{u_j' T'} = \frac{\nu_t}{Pr_t}\frac{\partial T}{\partial x_j} \tag{1}$$

It can be seen that the turbulent heat flux correlates with the turbulent kinematic viscosity ν_t, Pr_t, and temperature gradient $\partial T/\partial x_j$. This concept describes turbulence-driven thermal diffusion and critically influences thermal prediction accuracy. However, thermophysical property variations nonlinearly decouple analogies (e.g., ν_t/α_t) in model equations, introducing significant errors into thermal predictions. Current turbulent heat flux modeling methods include the Simple Gradient Diffusion Hypothesis (SGDH), Generalized Gradient Diffusion Hypothesis (GGDH), and Algebraic Heat Flux Model (AHFM) [12]. AHFM solves turbulent heat flux directly via algebraic equations and can combine with SGDH or GGDH [13,14], but research on AHFM remains limited, and its applicability across broader operating conditions needs further validation. Beyond these methods, Pr_t is also key to describing the

relative behaviors of turbulent heat and momentum transport [15,16]. Zhao et al. [17] noted that turbulence models often lack accuracy in thermal performance predictions under heat flux of at least 1.4×10^4 W/m^2, as a constant Pr_t fails to capture turbulent heat fluxes. Mohebbi and Bazargan [18] developed a two-dimensional numerical model to study the influence of Pr_t on momentum and energy transport in vertical tubes. They found that adopting Pr_t values lower than 0.9 could enhance the agreement with experimental data by around 30 % as the buoyancy force increases. High-fidelity DNS data also support this view. Liu et al. [19] integrated the Reynolds analogy into DNS studies and observed significant deviations of Pr_t from a constant value. It addresses the nonlinear deficiencies and represents a promising approach to improve thermal prediction. Bae [20] introduced a variable Pr_t model that adapts to physical properties and fluid-thermal variables, and it was found to reduce average temperature deviation by at least 15 % along y^+ direction within diameters ranging from 4.57 mm to 20 mm.

Currently, model accuracy is optimized by adjusting the values of Pr_t and developing Pr_t correlations. Studies have shown that buoyancy effect is closely related to Pr_t changes [18]. Bazargan [21] found that during heat transfer deterioration (HTD), the viscous sublayer expands, thereby delaying near-wall thermal diffusion and raising wall temperatures. Bae [20] have repeatedly confirmed a critical finding that the Pr_t is far <1 in the flow boundary layer. This phenomenon stands in marked contrast to the predictions of conventional theories, and its underlying cause is closely linked to the inherent limitations of the SGDH and GGDH. Constant Pr_t values, 0.85, 0.9 and 1.0, are widely adopted in the Reynolds analogy [22,23]. Mohseni and Bazargan [24] reported a Pr_t of approximately 0.9 for weak buoyancy flows, but it drops to 0.55 during a severe HTD condition. Moreover, Howell et al. [25,26] further showed that the heat transfer coefficient decreases significantly with increasing Pr_t in supercritical flows. These findings revealed that the limitations of SGDH and GGDH become more pronounced in supercritical flows. The resulting flow inhomogeneity and modified turbulence structure cause the transport pathways for momentum and heat to diverge. Thus, the linear relationship between turbulent fluxes and mean gradients no longer holds, which reduces the prediction accuracy of conventional turbulence models. Besides, researchers have also developed variable Pr_t correlations. Manda [27,28] emphasized buoyancy's critical role in supercritical flows and proposed a new Pr_t correlation. The Pr_t decreases with increasing buoyancy and show better agreement with experimental data. Tang et al. [29] developed a Pr_t model dependent on the molecular Prandtl number, and the results indicated that transitional Pr_t variations significantly affect thermal prediction. Specifically, increased Pr_t values inhibit turbulent mixing, which in turn triggers HTD. Du et al. [30] took a different approach, formulating a Pr_t model incorporating pressure, fluid properties and channel diameter, which successfully captures HTD onset. Despite extensive research, fixed Pr_t values fail to reflect continuous changes in turbulent transport characteristics, often causing abrupt discontinuities in physical quantities at sub-region boundaries and reducing prediction accuracy. Obviously, the full-field Pr_t correction research is therefore crucial, as it enables dynamic Pr_t adjustment with spatial variations. Importantly, it avoids property fragmentation from piecewise constant assumptions, and produces simulations that better reflect real flow and heat transfer processes, thereby providing a more robust numerical basis for engineering practice and scientific research.

In recent years, machine learning (ML) has advanced turbulence modeling significantly via two main methods [31]. The first method, direct learning, employs ML to model flow features from DNS or LES data to unclosed turbulence terms. Ellis et al. [32] created vector-based neural networks with expanded feature spaces that effectively replicated the complex trends of this vector, outperforming gradient diffusion models. Similarly, Sandberg et al. [33] used gene expression programming for nonlinear heat-flux closures, which greatly enhanced the prediction of adiabatic wall effectiveness. Milani et al. [34] introduced a technique where machine learning refines the turbulent diffusivity field within the SGDH form, significantly enhancing the predictions compared to typical RANS closures. Ellis and Xia [35] achieved this by combining a tensor-basis neural network for Reynolds stresses with their heat flux model, resulting in improved velocity, Reynolds stress, and temperature fields, and achieving advanced RANS predictions. Additionally, Ling and Templeton [36] highlighted machine learning's ability to identify unreliable RANS model regions, emphasizing the value of these data-driven techniques in model development and application. The second method, inverse learning, determines unclosed turbulence term distributions by solving inverse problems with time-averaged state data (e.g., velocity, temperature), on which ML models are trained. Parish et al. [37] introduced a framework combining flow inversion via the adjoint method. Holland et al. [38] enhanced this by creating a single-step method integrating inversion and ML training, reducing errors and boosting accuracy. Similarly, Zhang et al. [39] applied an adjoint-based single-step framework to develop ML-based turbulence models from LES temperature data. Duraisamy and colleagues [40,41] proposed a two-step framework using the discrete adjoint method to calculate the objective function gradients for unclosing terms. They later developed another two-step approach via the discrete adjoint method for gradient calculation, with these spatial distributions integrated into neural networks. Alternatively, Zhang et al. [42] and Wang et al. [43] used ensemble Kalman filter methods for inversion and turbulence model training. Overall, direct learning, using DNS or LES data, has been effective for predicting Reynolds stresses and heat fluxes but is limited in complex thermo-physical regimes like supercritical fluids due to data scarcity. Thus, inverse learning is more crucial, as it deduces spatial distributions of unclosed terms, such as the Pr_t from available data. Adjoint method frameworks are particularly effective, providing exact gradients for optimization at a cost similar to forward simulations, making them ideal for complex supercritical flow simulations where accurately determining a non-uniform Pr_t is essential.

This paper proposes an inverse adjoint learning framework to address the limitations of conventional RANS turbulence models—specifically, their inaccurate assumptions of constant thermophysical properties and flow isotropy. To improve prediction accuracy, the framework adjusts the nonlinear spatial Pr_t using local flow characteristics and integrates the adjusted Pr_t into a thermal diffusion equation. The process uses a coupled forward-inverse solution in Stanford University Unstructured (SU2) software controlled by Python, to optimize a loss function. Adjoint solutions then compute loss function gradients with respect to Pr_t at each grid point. These gradients directly update neural network parameters in the PyTorch framework. Additionally, a neural network model is also developed to link RANS flow features to LES temperature coordinates, creating a target Pr_t loss function to enhance turbulent thermal prediction.

2. Methodology

This section presents the adjoint-based inversion framework for creating a data-driven Pr_t model. The methodology comprises five steps: (1) defining the inversion parameter and strategy (Section 2.1); (2) formulating the adjoint-based inversion problem to assess the sensitivity of a temperature-matching objective function to the Pr_t field (Section 2.2); (3) detailing the iterative inversion process that integrates computational fluid dynamics (CFD) solvers with neural network training (Section 2.3); (4) selecting key input features from a supercritical fluid database (Section 2.4); and (5) developing a hybrid neural network to map these features to optimized Pr_t values (Section 2.5). The objective function is detailed in Section 2.6.

2.1. Inversion parameters

This subsection aims to define the inversion target parameter and justify the modeling strategy. Two main strategies correct turbulent thermal diffusion in RANS models: modifying diffusion intensity and developing anisotropic closures. The typical equation for the turbulent

temperature diffusion vector $\overline{u_k' T'}$relies on turbulent thermal diffusivity α_t, which is determined by the turbulent viscosity ν_t and Pr_t. The formula is as follows,

$$\overline{u_k' T'} = -\alpha_t \frac{\partial T}{\partial x_k} \tag{2}$$

$$\alpha_t = \frac{\nu_t}{Pr_t} \tag{3}$$

This study adopts the first strategy to optimize full-field Pr_t and better control turbulent thermal diffusion. As Ryan et al. [44] showed, incorporating α_t from LES data enables RANS temperature predictions to reach LES-level accuracy. This finding indicated that dynamically adjusting diffusion intensity significantly enhances prediction precision, even under the flow isotropy assumption. Notably, modeling Pr_t instead of α_t offers distinct advantages: it leverages ν_t, a native output of turbulence models. This not only simplifies physical parameter integration but also extends the framework's applicability to analogous thermal diffusion problems. This is because using the well-established ν_t reduces the need for problem-specific adjustments to α_t. Furthermore, although the SGDH is inherently isotropic, dynamically adjusting Pr_t allows the model to compensate for the effects exerted on the scalar (temperature) field by anisotropic processes. The dynamically adjusted Pr_t is incorporated directly into the energy equation through the α_t. As the energy equation is solved in its conserved form, global energy conservation is strictly maintained.

2.2. Adjoint inversion

This subsection describes how the adjoint method efficiently calculates the objective function to the Pr_t throughout the computational domain. This study employs an adjoint-based inversion method to efficiently calculate the gradient vector dJ/dPr_t, which reflects the sensitivity of the scalar objective function J to spatially distributed Pr_t across millions of grid points. The J represents the temperature prediction difference between LES and RANS models. By linearizing flow equations, the method formulates an adjoint problem—this allows determining the design variable field with a single adjoint solution. The SU2 discrete adjoint solver, a CFD tool, utilizes automatic differentiation for adjoint code generation, eliminating manual derivation and enhancing flexibility for user-defined goals [45,46]. It accurately computes the gradient dJ/dPr_t, which quantifies how local Pr_t changes affect J. The optimization process adjusts the Pr_t model to minimize J using LES temperature data, yielding corrected Pr_t-based RANS temperature that match LES accuracy. It involves linearizing the original nonlinear partial differential equations (PDEs) around a converged flow solution, forming a linear perturbation system. Adjoint variables measure the sensitivity of the objective function, J, to state variables such as velocity, pressure, and temperature. This sensitivity links to the linear system via an inner-product relationship, often established using Lagrange multipliers or variational principles. This process derives a linear PDE or algebraic system for adjoint variables, which remains linear even if the primal system is nonlinear. Boundary conditions depend on J's definition, such as wall heat flux. In discrete framework like SU2, discrete adjoint equations arise from the linearized conjugate transpose of discretized primal equations. Solving these equations with primal state derivatives enables efficient and precise gradient computation (dJ/dPr_t) for all design variables across millions of grid points without explicit perturbation solves. This is critical for computational efficiency in large-scale optimization and inversion problems.

The adjoint method's core is defining an objective function J and a state equation$R(U,\alpha) = 0$. The Lagrangian function, $L = J(U,\alpha) + \lambda^T R(U,\alpha)$, is constrained by the state equation $R(U,\alpha) = 0$, representing discretized RANS and energy equations. Here, U is the flow state vector, and α is the design variable vector. To compute the constrained gradient of J, a Lagrange multiplier vector λ, or adjoint variable, is employed. Setting the Lagrangian's derivative with respect to U to zero, $\frac{\partial \mathscr{L}}{\partial U} = \frac{\partial J}{\partial U} + \left(\frac{\partial R}{\partial U}\right)^T \lambda = 0$, forms the basis of the discrete adjoint equation, as follows,

$$\left(\frac{\partial R}{\partial U}\right)^T \lambda = -\frac{\partial J}{\partial U} \tag{4}$$

where $\partial R/\partial U$ is the Jacobian of the discretized governing equations, and $\partial J/\partial U$ shows J's sensitivity to state variables. Solving Eq. (4) for λ is essential for efficiently calculating the total gradient of J with respect to α, as follow,

$$\frac{dJ}{d\alpha} = \frac{\partial J}{\partial \alpha} + \lambda^T \frac{\partial R}{\partial \alpha} \tag{5}$$

Eq. (5) underpins the adjoint method's efficiency. Its computational complexity mainly lies in solving the adjoint Eq. (4). The computational cost for the terms $\frac{\partial J}{\partial \alpha}$ and $\frac{\partial R}{\partial \alpha}$ (direct sensitivities of design variables to the objective function and residuals) is typically far lower than that of the flow solution. Using SU2's automatic differentiation (AD), we solve discrete adjoint Eq. (4) automatically and generate Jacobian matrices ($\frac{\partial R}{\partial U}$and $\frac{\partial R}{\partial \alpha}$,) and sensitivity vectors ($\frac{\partial J}{\partial U}$ and $\frac{\partial J}{\partial \alpha}$) needed for gradient evaluation. This eliminates manual derivation, enabling efficient gradient computation $\frac{dJ}{d\alpha}$ for million-scale design variables Pr_t. These results are critical for inverse optimization of the Pr_t model.

2.3. Inversion process

This subsection details the iterative process that combines CFD solutions, adjoint-based gradient computation, and neural network training to learn the Pr_t model. Fig. 1 shows the inverse learning workflow, which couples the forward problem solving with the nonlinear neural network training of the Pr_t model, leveraging the SU2 software and PyTorch. The goal is to develop a neural network to predict Pr_t by minimizing a loss function based on high-fidelity LES temperature data, ensuring RANS simulations match LES data. Adjoint solutions derive loss function gradients for local Pr_t at each grid point, and PyTorch uses these gradients to optimize neural network parameters. The training process involves iterative cycles of forward simulation, inverse solution, and network updates, yielding a nonlinear mapping between flow features and Pr_t. This mapping produces an algebraic Pr_t model that adapts to diverse flow conditions and captures complex nonlinear supercritical flow behaviors.

The detailed iterative process, outlined in Fig. 2, is as follows:

(i) **Initialization**: The process begins by solving the forward RANS equations with a uniform initial guess for Pr_t (e.g., 0.85). The resulting flow field provides the initial input features for the neural network, which is likewise initialized to output a uniform Pr_t value.

(ii) **Forward solution**: In each iteration, the neural network predicts a Pr_t field from the latest flow features, followed by a forward RANS simulation to compute the flow state and objective function J.

(iii) **Inverse solution**: The adjoint problem (Eq. (4)) is solved to obtain the sensitivity of the objective function to the Pr_t field, denoted as dJ/dPr_t, at every grid point. This is accomplished using SU2's discrete adjoint solver.

(iv) **Neural network update**: The gradients dJ/dPr_t are back-propagated through the neural network using the chain rule to calculate gradients for the network's weights and biases. PyTorch then updates these parameters to minimize J in the next iteration.

(v) **Convergence check**: Steps (ii) to (iv) are repeated until the objective function J drops below a set threshold, indicating satisfactory agreement between RANS temperature predictions and LES reference data.

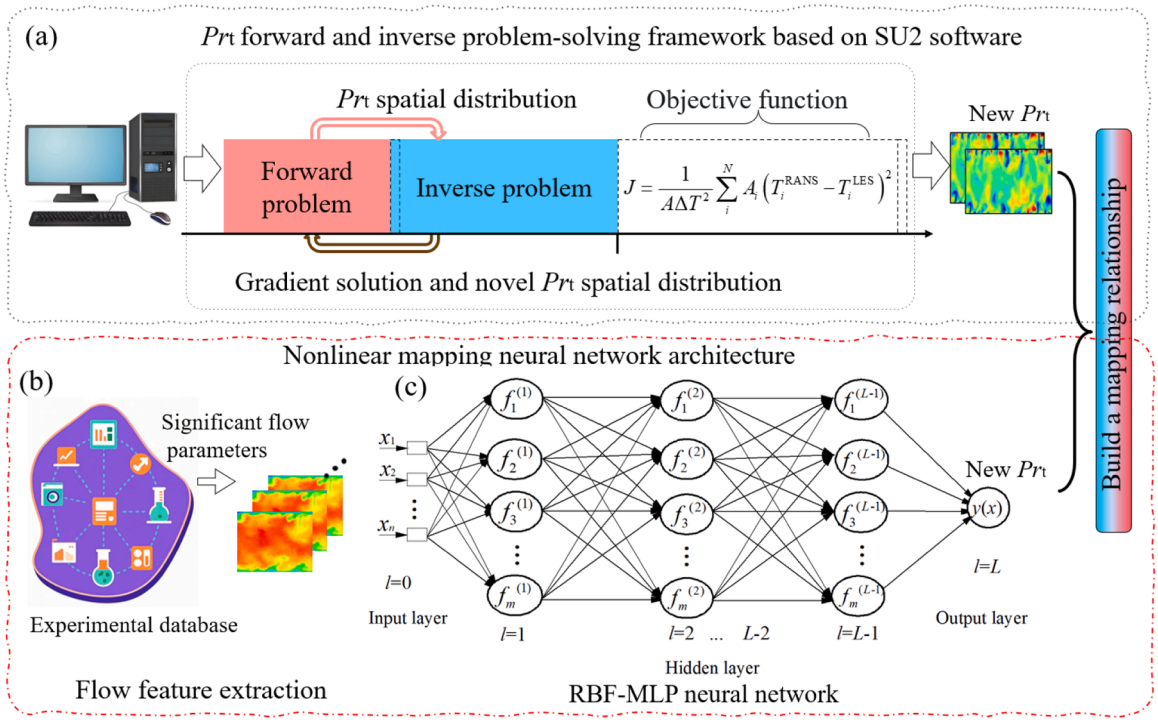


Fig. 1. Schematic of ML-based Pr_t inversion and mapping with three components: (a) SU2 forward solution and adjoint-based Pr_t inversion using a loss function with LES temperature data for gradient computation; (b) extraction of dominant flow and thermal features from a supercritical experimental database; (c) a hybrid RBF-MLP network predicting Pr_t from features, showcasing nonlinear algebraic modeling.

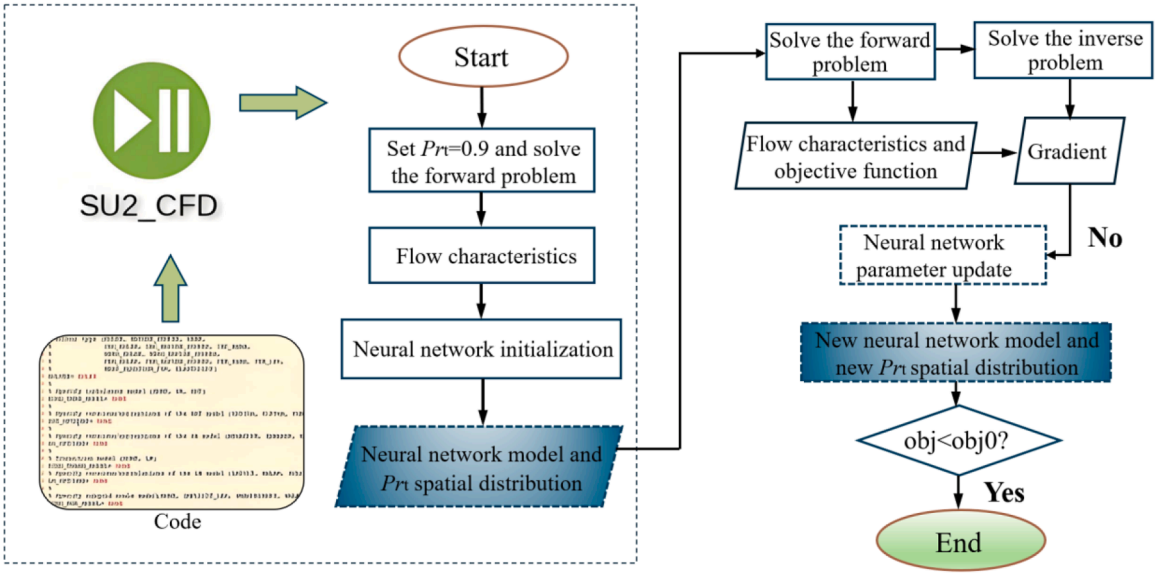


Fig. 2. Workflow of Pr_t inversion adjoint and flow feature mapping of neural network based on the SU2 platform.

2.4. Feature extraction

This subsection describes the rationale and process for choosing neural network input features from various potential parameters. Selecting input features for the neural network is crucial for model generalization beyond the training LES case. We use a broad experimental data set to identify key parameters, preventing the model from focusing on simulation-specific features and ensuring it captures essential thermo-physical relationships in various supercritical flows. Hence, experimental data from various operating conditions serve as ground-truth samples for model training and testing. It is critical for capturing complex physics and correlating intricate thermofluidic features. In previous studies [47], we compiled 11,852 experimental data points from public sources, covering fluids like supercritical carbon dioxide (CO_2), hydrocarbon fuels, H_2O, and R134a. This database is now essential for developing and validating advanced ML models.

Specifically, experiments were conducted under pressures of 4.3–32 MPa, mass fluxes of 200–2021 kg/(m^2·s), heat fluxes of 0.2–1385 kW/m^2, and channel diameters of 4.4–26 mm. Measured parameters included outer-wall temperatures (T_w), convective heat transfer coefficients (h), and dimensionless wall Nusselt numbers (Nu). All supercritical fluids exhibit significant thermophysical property changes near

critical points, leading to similar flow and heat transfer behaviors. Heat transfer influences fall into two broad categories. First are boundary and geometric parameters, including mass flow rate (G), operating pressure (P), inlet temperature (T), inlet enthalpy (h_b), heat flux (q) and inner diameter of channel (d_{in}). Second are flow regime and thermophysical property parameters, including bulk Reynolds number (Re_b, quantifying the ratio of inertial to viscous forces), bulk Prandtl number (Pr_b, describing the relative diffusion of momentum and heat), wall Reynolds number (Re_w), wall Prandtl number (Pr_w), bulk Grashof number (Gr_b, characterizing natural convection effects), modified bulk Grashof number (Gr_b*, characterizing buoyancy-induced flow), bulk-to-wall density ratio (ρ_b/ρ_w), bulk-to-wall thermal conductivity ratio (λ_b/λ_w), bulk-to-wall dynamic viscosity ratio (μ_b/μ_w), bulk-to-wall specific heat capacity ratio ($c_{p,b}/c_{p,w}$), normalized bulk heat flux (q_b^+), flow acceleration term (Ac), buoyancy factor term (Bu and Bo*).

The T_w, h and Nu are measured outside the channel, while internal pressure remains constant in channels. Using National Institute of Standards and Technology (NIST) software, the primary fluid's enthalpy is converted to temperature for direct comparison with wall temperatures. Thus, all thermophysical properties can be derived from flow pressure and temperature data, ensuring generality. Key parameters influencing flow and heat transfer behaviors are extracted as inputs to the RBF-MLP network, which maps them to the output parameter Pr_t.

Key parameter identification methods include grey relational analysis, partial least squares regression, and the Pearson correlation coefficient method. The Pearson method is chosen for further feature analysis due to its ability to quantify the direction and strength of linear correlations and facilitate fast batch calculations. To identify parameters significantly affecting h, Pearson correlation and significance value (P-value) are calculated for each parameter using n data point pairs (x_1,y_1), …,(x_n,y_n). The P-value calculation is as follows,

$$P = \frac{\sum_{i=1}^{n}(x_i-\bar{x})(y_i-\bar{y})}{\sqrt{\sum_{i=1}^{n}(x_i-\bar{x})^2\sum_{i=1}^{n}(y_i-\bar{y})^2}} \tag{6}$$

The P-value quantifies correlation strength and ranges from −1 to 1. Values near −1 or 1 indicate a strong linear correlation, while those near 0 indicate a weak one. Detailed results are provided in Table 1.

The top five features, Pr_w, G, Pr_b, q, and ρ_w/ρ_b, are chosen as inputs to the RBF-MLP neural network. The Pr_w with a coefficient of 0.739, exerts the strongest positive influence on the heat transfer coefficient. The G with a coefficient of 0.591, affects flow regimes and momentum transport efficiency. The Pr_b with a coefficient of 0.509, characterizes bulk fluid properties and turbulent heat exchange. The q with a coefficient of 0.357, signals heat transfer risks and defines operational limits. The ρ_w/ρ_b with a coefficient of 0.295, captures density variation's influence on buoyancy effects and flow regimes. These parameters collectively cover key flow characteristic aspects, so they are chosen as the input variables. After training, the model effectively learns flow-thermal coupling mechanisms, enabling accurate performance predictions under complex supercritical conditions.

Table 1
P-values and correlation analysis of key parameters influencing heat transfer behaviors.

Feature Parameter	P-value	Correlation and Influence
Pr_w	0.739	Positively correlated; exerts the most significant influence on the heat transfer coefficient.
G	0.591	Positively correlated; notably affects flow and heat transfer regimes.
Pr_b	0.509	Positively correlated; reflects the impact of thermophysical properties on heat transfer.
q	0.357	Positively correlated; high heat flux tends to induce heat transfer deterioration.
ρ_w/ρ_b	0.295	Positively correlated; reflects how density change impacts buoyancy and flow states.
Re_w	0.207	Positively correlated; embodies the role of wall-side flow states.
$c_{p,w}/c_{p,b}$	0.141	Positively correlated; associated with thermal boundary layer characteristics.
μ_w/μ_b	0.110	Positively correlated; influences the distribution of viscous forces within the boundary layer.
Re_b	0.073	Positively correlated; reflects the turbulence degree in the bulk flow.

2.5. Mapping neural network

This subsection describes the nonlinear hybrid structure for mapping flow features to Pr_t and justifies its suitability. Supercritical fluid data is high-dimensional and nonlinear, which typically requires deep learning networks with numerous layers and neurons. However, this section proposes a simpler yet powerful nonlinear structure suitable for fast engineering computations. Our previous work developed a hybrid RBF-MLP neural network, detailed in Ref. [31], which combines the local feature extraction of Radial Basis Functions (RBF) and the global nonlinear mapping of Multilayer Perceptrons (MLP), as shown in Fig. 3. It improves performance in complex tasks, such as classification, regression, and function approximation.

The mathematical expression of the first network layer is,

$$y^1(x) = \sum_{i=1}^{n} w_i^1 \varphi^1\left(\| x - c_i^1 \|, \sigma_i^1\right) = \sum_{i=1}^{n} w_i^1 \exp\left(-\frac{\| x - c_i^1 \|^2}{2\sigma_{1i}^2}\right), i = 0, \ldots, n. \tag{7}$$

and that for the second layer is,

$$y^2(x) = \sum_{i=1}^{n} w_i^2 \varphi^2\left(\| x - c_i^2 \|, \sigma_i^2\right) = \sum_{i=1}^{n} w_i^2 \exp\left(-\frac{\| x - c_i^2 \|^2}{2\sigma_{2i}^2}\right), i = 0, \ldots, n. \tag{8}$$

Iterative application of this process ultimately yields the RBF-MLP model, which takes the form $y(x) = f^1(x) + f^2(x) + \ldots + f^k(x)$. Moreover, all layer weights (w) can be determined via the least squares method. The RBF layer, placed at the front end, receives input data. It uses radial basis functions (e.g., Gaussian kernel) to calculate the distance between the input and hidden-layer center points, generating local response features. Notably, it excels at capturing local patterns and data clustering features.

This neural network offers three key advantages for modeling supercritical flow. 1) The RBF layer automatically extracts local features, reducing the MLP's learning load; 2) It mitigates the curse of dimensionality by reducing dimensions before data enters the MLP, easing high-dimensional input challenges and avoiding overfitting; 3) Its local response mechanism enhances robustness to noise and outliers. The RBF-MLP's staged feature learning combines local response and global mapping, making it ideal for tasks that require local pattern recognition and handling complex nonlinearities. Table 2 presents the RBF-MLP model's parameter settings and accuracy results. The RBF-MLP neural network consists of 5 layers in total. Specifically, there are 3 hidden neuron layers, each with 20 nodes. The activation function for the output layer is Purelin, while the hidden layers employ the RBF activation function. It achieved a maximum regression coefficient of 0.99 and an RMSE below 1 %. The model also effectively captured turbulent fluctuations, even with high nonlinear buoyance force. For more details on the model's architecture, please refer to Ref. [31]. Besides, the data division strategy and convergence results are presented and discussed in Section 4.1.

2.6. Objective function

This subsection aims to formally define the objective function that

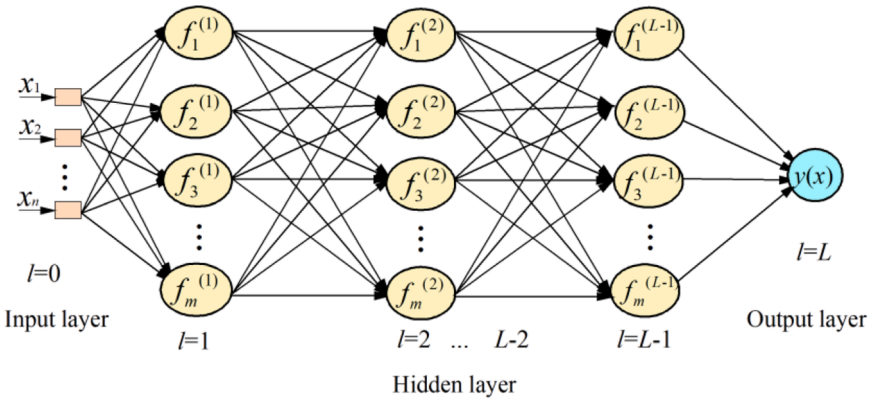


Fig. 3. Schematic diagram of the RBF-MLP Model.

Table 2
Model parameter settings and accuracy results of the RBF-MLP model.

No.	Corresponding parameter	Option or value
1	No. layer	5
2	No. hidden neuron layer	20+20+20
3	Output layer activation function	Purelin
4	Hidden layer activation function	RBF
5	Training and test subsets	80 % and 20 %
6	Regression coefficients, R	0.99

measures the discrepancy between RANS and LES results, guiding the inversion process. The adjoint solution employed in this paper is implemented via the open-source software SU2. Its core function is to compute the gradient of a scalar objective function with respect to any number of design variables in a single adjoint solution process. Notably, SU2's discrete adjoint solver uses automatic differentiation, allowing users to define objective functions and design variables without embedding adjoint equations. The objective function J is defined as the difference between predicted temperatures from LES and RANS data on the symmetry plane and wall surface, expressed as,

$$J = \frac{1}{A\Delta T^2}\sum_{i}^{N} A_i\left(T_i^{\mathrm{RANS}} - T_i^{\mathrm{LES}}\right)^2 \tag{9}$$

where A_i is the area of a surface grid cell, A is the total area of the target region, and ΔT is the temperature difference. Minimizing J aligns RANS predictions with LES data. The design variable is $Pr_t \in \mathrm{R}^n$, defined at all grid points. The gradient vector $\mathrm{d}J/\mathrm{d}Pr_t$ is computed via a single adjoint solution in SU2's adjoint solver.

This study employs three quantitative error metrics to evaluate model performance: the pointwise relative error (e_i) to quantify local deviations, the mean absolute relative error (e_R) to measure the global average deviation, and the root mean-square relative error (e_S) to penalize larger errors due to its quadratic weighting. The corresponding formulas are given below,

$$e_i = \frac{y_{\mathrm{pred}} - y_{\mathrm{ref}}}{y_{\mathrm{ref}}} \times 100\% \tag{10}$$

$$e_R = \frac{1}{n}\sum_{i=1}^{n}|e_i| \times 100\% \tag{11}$$

$$e_S = \sqrt{\frac{1}{n}\sum_{i=1}^{n}|e_i|^2} \times 100\% \tag{12}$$

where y_{ref} denotes experimental or LES reference data, while y_{pred} signifies values computed by turbulence or ML-based models.

3. Physical model and working fluid

The physical model configuration strongly influences flow, heat transfer behaviors. This study compares sCO_2 in circular channels with supercritical hydrogen fuel in rectangular channels to select a configuration-fluid pair for validating the ML-Pr_t model. Fig. 4 presents the previous finding that while the two channel types exhibit similar flow and heat transfer characteristics, configuration significantly impacts supercritical flow and heat transfer [48,49]. A key difference is that asymmetric rectangular heating channels with high heat flux induce more wall-near disturbances and complex variations than uniformly heated circular channels. To validate the ML-Pr_t model, subsequent work will use a rectangular channel and supercritical hydrocarbon fuel.

This study uses a mesh system with tens of millions (10^8) of grids to iteratively refine RANS solutions towards the LES target. The mesh setup has been validated in our previous supercritical work in Ref. [4]. The key mesh parameters are set with $y^+<1$, span-wise resolution Δz^+ of 20, and stream-wise resolution Δx^+ of 13. It includes highly refined near-wall regions and a structured layout for resolving complex flow structures. Further details can be found in Ref. [4].

Notably, hydrocarbon fuels composed of chain hydrocarbons, naphthenes, and aromatics, exhibit thermophysical properties similar to n-decane, making n-decane a suitable fluid medium for numerical simulations. These fuels crack into smaller molecules at 750–770 K. For computational efficiency, this study uses the Proportional Product Distribution (PDD) cracking model for LES and SU2 simulations of supercritical n-decane. The PDD equation is,

$$\begin{aligned} C_{10}H_{22} \rightarrow\ & 0.15H_2 + 0.143CH_4 + 0.256C_2H_4 + 0.126C_2H_6 + 0.230C_3H_6 \\ & + 0.180C_3H_8 + 0.196C_4H_8 + 0.102C_4H_{10} + 0.171C_5H_{10} + 0.124C_5H_{12} \\ & + 0.195C_6H_{12} + 0.089C_6H_{14} + 0.169C_7H_{14} + 0.072C_7H_{16} + 0.152C_8H_{16} \\ & + 0.012C_8H_{18} + 0.053C_9H_{18} + 0.003C_9H_{20} \end{aligned} \tag{13}$$

The reaction rate of the thermal cracking of supercritical n-decane is given by,

$$\omega_R = dC_R/dt = -KC_R \tag{14}$$

$$K = k_0 \cdot \exp\left(-\frac{E_a}{RT}\right) \tag{15}$$

where ω_R is the reaction rate (mol/m^3·s), C_R is the reactant concentration (mol/m^3), t is the time (s), K is the rate constant (s^{-1}), k_0 is the pre-exponential factor (1.6×10^{15} s^{-1}), and E_a is the activation energy (263.7 kJ/mol).

In simulation, thermophysical properties are sourced from NIST database. The solid material, stainless steel, has a density of 7930 kg/m^3, a specific heat capacity of 500 J/(kg·K), and a thermal conductivity that ranges from 12.1 to 28.5 W/(m·K) as temperature increases. The

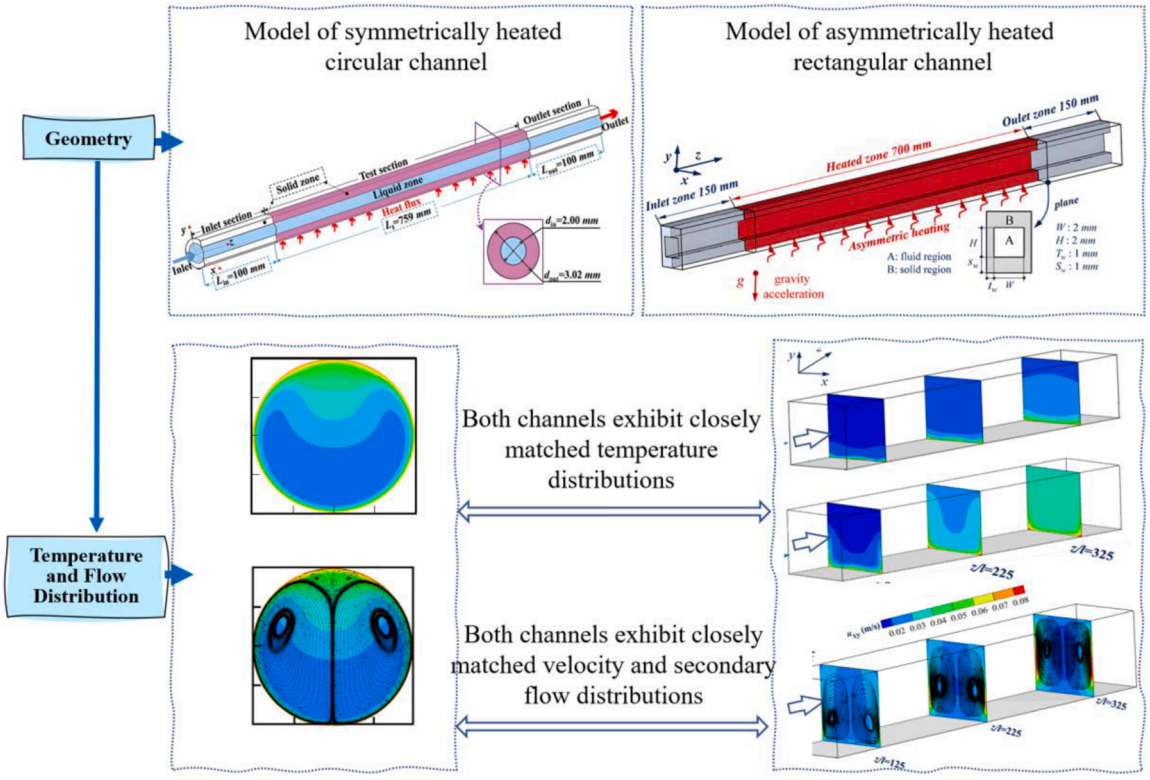


Fig. 4. Analysis of flow and heat transfer characteristics of supercritical fluids flowing in different channels [48,49].

rectangular channel model uses the following settings: inlet temperature 300 K, mass flow rate 2 g/s, and outflow boundary condition at the outlet. Gravity is set to 9.8 m/s^2, and a heat flux density of 1.5 MW/m^2 is applied to the combustion chamber wall. This study adopts a data-driven modeling approach, which relies on high-fidelity data. While DNS produces the most accurate data, it is computationally expensive. By contrast, LES is a more efficient alternative—it captures small-scale turbulence at lower computational cost. Thus, LES data of high-dimensional hydrocarbon fuel flow in the regenerative cooling channel of a scramjet engine are used as the target flow data.

4. Results and discussion

The computational accuracy of ML models is validated by training

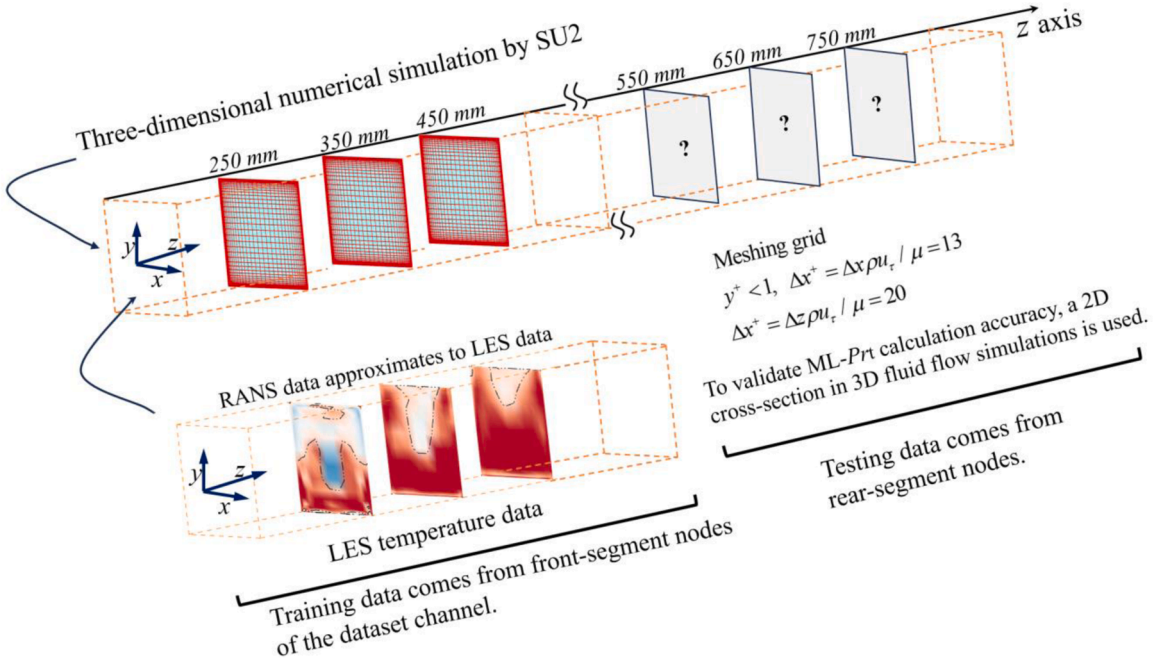


Fig. 5. Dataset dividing for Pr_t inversion, where training data are sourced from nodes in the first half of the channel, test data from the second half, and the model is developed via comparing ML predictions with high-fidelity LES data and assessed for generalization and accuracy using the test set.

them on a given dataset and evaluating their prediction performance on an independent test dataset. Specifically, if the Pr_t derived via inverse adjoint methods exhibits high accuracy on the test dataset across various operating conditions—even with limited training data—it directly confirms the strong generalization capability of the ML-based Pr_t model. Furthermore, using sensitive key flow and heat transfer parameters as monitoring metrics is critical for comprehensively evaluating the model's computational accuracy. These parameters effectively capture subtle discrepancies between predicted and actual flow data.

4.1. Training and testing

Fig. 5 illustrates the dataset selection method for the Pr_t inversion process. The dataset, extracted from LES data of supercritical n-decane in a non-uniformly heated rectangular channel, is divided into training and test sets. The training set, comprising data from the first half of the channel's axial section, allows the Pr_t model to analyse the non-linear flow evolution. The test set, derived from the second half, validates the model's generalization and accuracy by comparing predictions with high-fidelity LES data.

Fig. 6 depicts the convergence trajectory of the inverse learning process. Each iteration requires solving both forward and inverse problems. The horizontal axis shows training iteration steps, while the vertical axis indicates the objective function value, J. The objective function reaches 0.008 after 20 iterations, and the model fully converges at approximately the 46th iteration with a value of 5×10^{-4}. It is significantly faster than the usual thousands of iterations in typical deep learning training. This rapid convergence is due to a noise-free deterministic parameter-objective mapping, integration of global mesh element information in each iteration, and simplified optimization through direct parameter estimation. Thus, compared to conventional neural networks, this model has effectively alleviated the issue of excessive computational cost.

4.2. Inversion results of Pr_t

Fig. 7 presents the distributions of Pr_t inverted at $z = 250$ mm, 350 mm, 450 mm, 550 mm, 650 mm, and 750 mm. It is shown that the values of ML-based Pr_t model are generally below 0.75, which aligns well with findings in the Ref. [50] suggesting that Pr_t settings between 0.5 and 0.6 closely match experimental data. In terms of its overall distribution, a robust dual-layer structure is universally observed at all planes. The turbulent core region is characterized by a stable, low-value Pr_t plateau (approximately 0.35–0.50), while the near-wall region features a sharp, non-linear increase to a peak between 0.50 and 0.75. This phenomenon arises from the interplay of significant property variations and buoyancy, particularly near the pseudo-critical point, which alters turbulence and reduces momentum transport efficiency compared to heat transport. This decoupling is quantitatively indicated by a sharp increase in Pr_t in the near-wall region. The universal double-layer structure shows that assuming a constant Pr_t for strong convective heat transfer at supercritical pressure is invalid, highlighting the need for a variable Pr_t model to analyze near-wall physics decoupling.

At the channel entrance, the thermal boundary layer is forming, with a significant and concentrated Pr_t peak near the wall due to recent intense heating, causing a strong initial separation of momentum and heat transport. The low Pr_t value in the core area may not be fully developed yet. As the flow moves downstream, the thermal boundary layer thickens, and the large Pr_t extends towards the turbulent center. The bilayer structure of Pr_t remains intact, with a consistently sharp upward trend in the near-wall region, despite slight changes in peak height. This suggests that the decoupling of turbulent transport due to variable physical properties is a persistent, steady-state phenomenon throughout the heating section, not just a transient or inlet effect. This study reveals the intricate spatial evolution of Pr_t in supercritical fluid heat transfer, challenging the constant Pr_t model with its universal double-layer structure and axial persistence. It offers crucial insights and validation data for advancing high-precision supercritical flow heat transfer models.

4.3. Prediction results

The Pr_t quantifies the efficiency of turbulent heat transport relative to turbulent momentum transport, thus governing turbulent thermal diffusivity. In typical turbulence models, turbulent viscosity, ν_t, is calculated independently and is unaffected by Pr_t. Thus, changing Pr_t cannot directly impact flow results, such as velocity and pressure. Instead, changes occur indirectly through temperature variations that affect thermophysical properties or buoyancy coupling mechanisms. In the near-wall region, large temperature gradients indirectly influence flow distribution, creating a flow-thermal coupling effect until equilibrium is reached. Table 3 lists key parameters affected by Pr_t changes.

Herein, α_t is crucial in turbulence models, as it affects the temperature-related quantities. Indirectly influenced parameters are selected as monitoring variables—this is because discrepancies between ML predictions and LES results better reflect the Pr_t model's generalization ability. Specifically, the monitored variables include Reynolds number (Re), Grashof number (Gr_b), shear production term (P_s), and buoyancy production term (P_b). Re quantifies the ratio of inertial to viscous forces. A large temperature gradient increases the density gradient, which indirectly raises Re. It also causes fluid expansion, increasing Gr_b—a parameter that evaluates buoyancy effects. The equations are defined as follows,

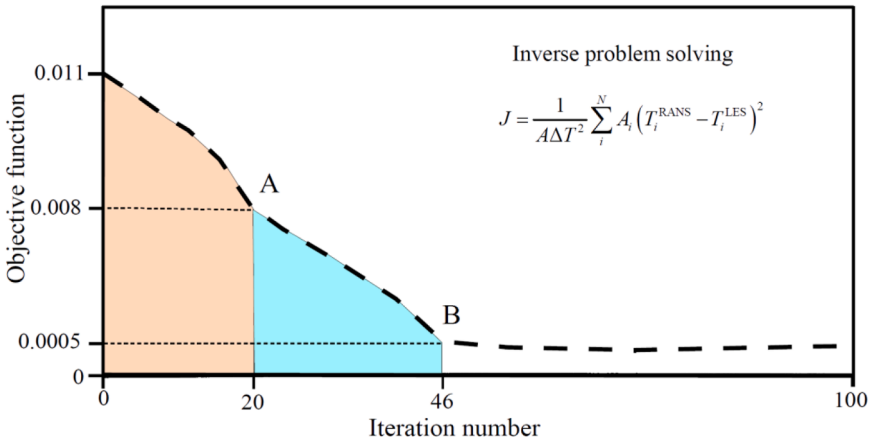


Fig. 6. Convergence history of ML-based inverse learning.

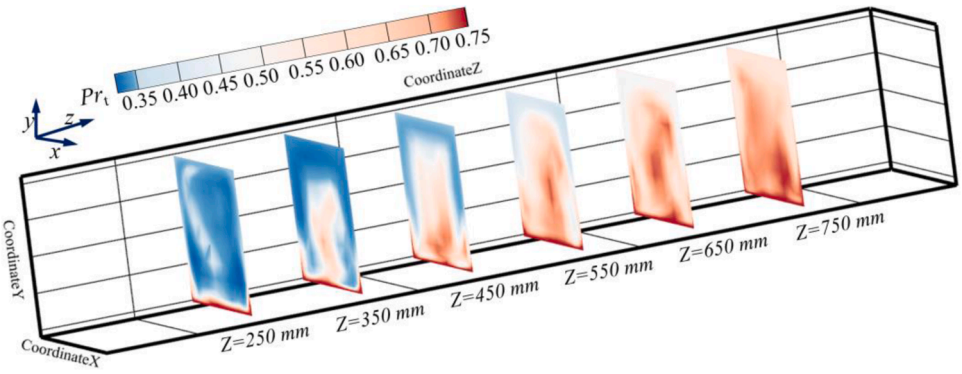


Fig. 7. Full-field Pr_t distribution contour obtained from the ML-based inversion model.

Table 3
Classification of parameters influencing turbulent thermal diffusivity α_t.

Direct impact	Indirect impact
Temperature distribution (T) and gradient (∇T)	Reynolds number, $Re = \frac{\rho v L}{\mu}$
Wall heat flux, q_w	Grashof number, $Gr_b = -\beta g_i \frac{\mu_t}{Pr_t}\frac{\partial T}{\partial x_i} \propto \frac{\nu_t}{\alpha_t}\frac{\partial T}{\partial x_i}$
Turbulent heat flux, q_t	Turbulent shear production, $P_s = -\overline{u'v'}\frac{\partial \bar{u}}{\partial y}$ (simplified)
	Buoyancy production term, $P_b = -\frac{g}{\rho}\overline{\rho' v'}$ (simplified)
	Production/dissipation of turbulent kinetic energy k, P_k(production), ε(dissipation)

$$Re = \frac{\rho v l}{\mu} \tag{16}$$

$$Gr_b = -\beta g_i \frac{\mu_t}{Pr_t}\frac{\partial T}{\partial x_i} \propto \frac{\nu_t}{\alpha_t}\frac{\partial T}{\partial x_i} \tag{17}$$

where α_t indirectly affects Gr_b via the temperature gradient $\partial T/\partial xi$. Since $\alpha_t = \nu_t/Pr_t$, changes in α_t indirectly alter Gr_b. Here, ρ is fluid density (kg/m^3); ν is velocity (m/s); l is characteristic length (m); μ is dynamic viscosity (Pa·s).

Fig. 8 compares results from LES data, a conventional turbulence model (Pr_t=0.85), and an ML-based Pr_t model across cross-sections at Z = 250 mm, Z = 350 mm, Z = 450 mm, Z = 550 mm, Z = 650 mm, Z = 750 mm. Notably, numerous studies have shown that the SST k-ω model outperforms the two-equations k-ε models in resolving near-wall dynamics [2,49]. Thus, it is selected herein as the sole representative of conventional turbulence models fixed Pr_t=0.85. Below is a detailed analysis for each section. As shown in Fig. 8(a), at Z = 250 mm, the LES Re data rise sharply near the wall first, then decrease gently farther away—driven by disturbances and boundary layer development. The conventional SST k-ω model fixed Pr_t=0.85 deviates significantly from LES data, though this deviation is less pronounced in the upper-middle y-axis region. The ML-based Pr_t model follows the LES trend closely and shows small differences near y=−1 due to limited training data. At Z = 350 mm, the LES data curve fluctuates. The ML-based Pr_t model tracks these changes accurately, especially near the bottom and across the entire flow field. In contrast, the conventional model shows obvious large difference particularly near the wall, even though it captures the general fluctuation trend. At Z = 450 mm, the ML-based Pr_t model accurately captures Re variation near the bottom wall. The constant-Pr_t model fails to reflect nonlinear flow variations, showing significant differences from LES data. These results indicate the ML-based Pr_t model—by leveraging its robust nonlinear mapping capability—learns nonlinear Pr_t characteristics from LES data during inversion. At Z = 550 mm, the LES data curve rises steadily, and the ML-based Pr_t model

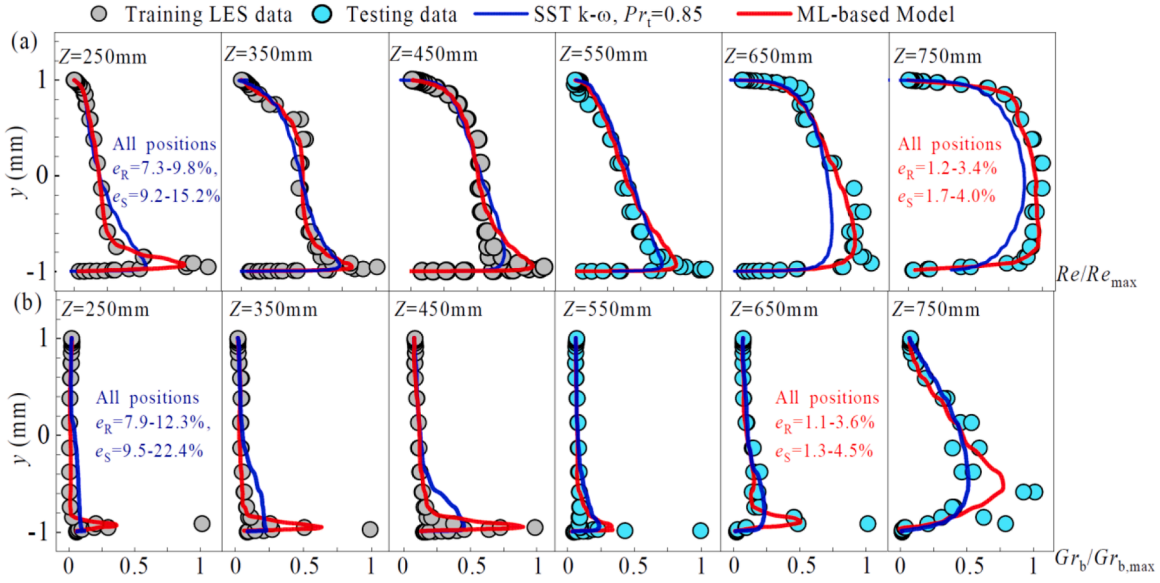


Fig. 8. Comparative analysis of data trends: (a) Re and (b) Gr_b under conventional Pr_t=0.85, ML-based Pr_t, and high-fidelity LES on the dataset. comparisons at Z = 250 mm, Z = 350 mm, and Z = 450 mm are based on the training set; those at Z = 550 mm, Z = 650 mm, and Z = 750 mm are on the test set.

matches it closely, while the conventional model deviates near $y=-1$. At $Z = 650$ mm and $Z = 750$ mm, the LES data fluctuate slightly, which is primarily attributed to the development of stronger buoyancy-driven instabilities and more complex flow structures in the further downstream region. The intrinsic flow characteristics increase unpredictability, causing higher local prediction errors in both the ML-based and constant-Pr_t models. However, our ML-based model better captures the overall flow trend, demonstrating its robustness in complex, unstable scenarios. The quantitative error metrics also confirm the marked superiority of the ML-based model over the conventional model at all evaluated positions. The conventional model has e_R and e_S ranges of 7.3–9.8 % and 9.2–15.2 %, respectively. In contrast, the ML-based model significantly reduces these errors to 1.2–3.4 % and 1.7–4.0 %, demonstrating its enhanced accuracy and robustness.

The Gr_b, an indicator of natural-convection buoyancy, is influenced by the temperature gradient determined by Pr_t. Thus, tracking Gr_b change can reflect the ML model's precision for Pr_t and indirectly assess the computational accuracy of flow information. Fig. 8(b) illustrates that at $Z = 250$ mm, $Z = 350$ mm and $Z = 450$ mm, the ML-Pr_t effectively captures the buoyancy-driven accelerated flow in the near-wall region, as indicated by a sharp Gr_b increase. Between $y = 0$ and $y = 1$ (weak buoyancy), both the ML-based Pr_t model and conventional model achieve high prediction accuracy. In the test set of $Z = 550$ mm and $Z = 650$ mm, as buoyancy develops from the bottom to the central turbulent region, the ML-based Pr_t outperforms the conventional model in prediction accuracy. At $Z = 750$ mm, despite increased difference due to large buoyancy disturbances and irregular Gr_b changes, the ML-based model still captures the y-axis trend of Gr_b. This confirms the model's effectiveness in using LES data to adjust Pr_t and track flow development. In contrast, the Pr_t=0.85 model fails to capture near-wall variation trends and deviates significantly from LES data—except between $y = 0$ and $y = 1$ (weak buoyancy), where its trend and accuracy align better. Based on the comprehensive error analysis across all measurement positions ($Z = 250$ mm to $Z = 750$ mm), the ML-based model also demonstrates remarkable accuracy and consistency. The conventional model exhibits significantly larger error ranges, with absolute relative errors e_R between 7.9–12.3 % and e_S spanning 9.5–22.4 %. In contrast, the ML model maintains lower errors, with e_R confined to just 1.1–3.6 % and e_S limited to 1.3–4.5 %. It reduces errors by 70–85 % compared to the conventional model. This highlights its superior predictive capability and reliability in capturing complex flow characteristics, with a consistently narrow error range indicating robustness and generalizability.

Herein, calculations focus on complex buoyancy-dominated indirect production terms to assess the accuracy of the ML-based Pr_t model. The shear production term, P_s, describes turbulence energy gain from the main flow via velocity gradients. The buoyancy production term, P_b, indicates buoyancy's effect on turbulent kinetic energy. It acts as either a production or dissipation term, depending on flow stability. These two terms represent the primary mechanisms for turbulent energy acquisition from the mean flow. Their formulas are provided as follows,

$$P_s = -\rho\overline{u'_i u'_j}\frac{\partial u_i}{\partial x_j} \tag{18}$$

$$P_b = -g\overline{\rho u'_j} \tag{19}$$

Fig. 9 compares prediction results from LES data, the conventional model fixed Pr_t=0.85, and the ML-based Pr_t model at the plane of $Z = 250$ mm, $Z = 350$ mm, $Z = 450$ mm, $Z = 550$ mm, $Z = 650$ mm and $Z = 750$ mm. A detailed analysis of each cross-section follows below. As shown in Fig. 9(a), at the $Z = 250$ mm, the LES data shows significant fluctuations in both bottom and top regions, and the conventional model fails to capture this behavior. In contrast, the ML-based Pr_t model accurately tracks the P_s trend along the y-axis. This indicates its ability to adjust Pr_t values across the domain and closely approximate LES velocity shear, enabling precise P_s predictions. From $Z = 350$ mm to $Z = 750$ mm, P_s fluctuations intensify along the flow direction. The conventional model poorly predicts these irregularities, as a constant Pr_t cannot adequately describe actual flow behaviors. The ML-based Pr_t model effectively captures the nonlinear characteristics of LES data along the y-axis, though discrepancies increase at certain locations—possibly due to limited data samples, leading to suboptimal predictions. A comparison of error metrics shows that the conventional SST k-ω model has large e_R and e_S ranges of 13.3–21.2 % and 15.5–26.4 %, respectively, whereas the ML-based model reduces these errors to ranges of 3.1–9.1 % for e_R and 4.3–10.1 % for e_S. Notably, the ML model maintains its accuracy even in complex near-wall buoyancy-driven flows. As shown in Fig. 9(b), at the $Z = 250$ mm, LES shows significant buoyancy production fluctuations near the bottom, with intense peaks. The conventional model fixed Pr_t=0.85 fails to capture these fluctuations, producing an overly

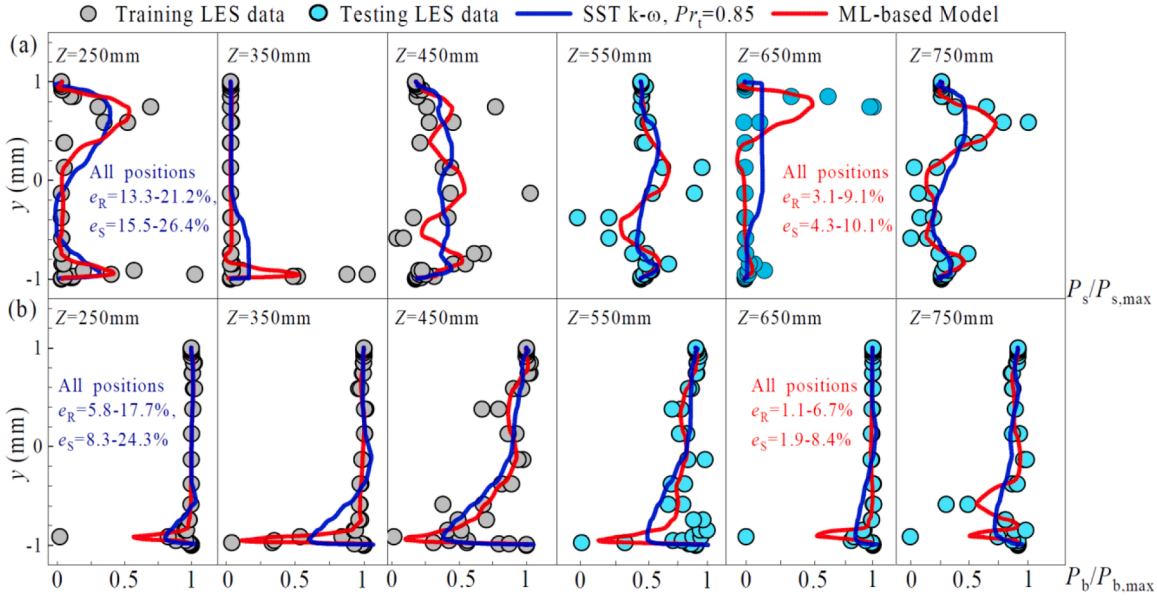


Fig. 9. Comparative analysis of data trends: (a) P_s and (b) P_b under conventional Pr_t=0.85, ML-based Pr_t, and high-fidelity LES on the dataset. Comparisons at $Z = 250$ mm, $Z = 350$ mm, and $Z = 450$ mm are conducted on the training set; Those at $Z = 550$ mm, $Z = 650$ mm, and $Z = 750$ mm are on the test set.

smooth curve. In contrast, the ML-based variable Pr_t model successfully replicates both the overall trend and key fluctuations of P_b from LES along the *y*-axis. A comparison of the error metrics demonstrates that the ML-based model achieves a significant improvement in accuracy over the conventional SST k-ω model. It reduces the error ranges from e_R=5.8–17.7 % and e_S=8.3–24.3 % to e_R=1.1–6.7 % and e_S=1.9–8.4 %. This superior predictive accuracy is maintained even in the presence of complex, buoyancy-driven flows near the wall. The results confirm that the ML-based Pr_t model, by dynamically adjusting Pr_t values, effectively captures the turbulent transport response to buoyancy forces and closely matches the spatial distribution of the LES reference solution.

Overall, the ML-based model outperforms the conventional model in handling LES fluctuations. It learns embedded physical information from high-fidelity LES data and dynamically adjusts Pr_t based on complex turbulent thermal characteristics, rather than relying on a constant value. This data-driven approach enables more accurate capture of turbulent heat flux behaviors, except near walls. Notably, future work should expand training data coverage to improve accuracy.

4.4. Comparison with experimental data

The training data are sourced from the first half of the horizontal rectangular channel (please see Fig. 5). Training proceeds until the objective function (Eq. (5)) falls below a set threshold—this aligns the RANS temperature distribution from SU2 with LES results, completing the learning process. This neural network predicts Pr_t from flow characteristics, forming a new data-driven turbulent thermal diffusion model. It is applied to a new test case to calculate flow and temperature fields. To verify the precision accuracy in circular channels, experimental data from published literature are used, and validation scenarios are categorized by flow direction.

4.4.1. Cross-condition validation: mass flow rate and heat flux variations in rectangular channels

To validate the precision accuracy of ML-based model under extreme trans-critical temperatures, two experimental datasets, Test 1 and Test 2, from Ref. [51] are used. Experimental conditions are detailed in Table 4. The test section uses a 1Cr18Ni9Ti electric heating channel with inner diameter of 1.5 mm, outer diameter of 3.0 mm, and length of 1.3 m. Wall temperature was measured via 16 K-type thermocouples on the channel's outer wall. Under an operating pressure (P_{in}) of 4 MPa, the critical temperature, T_{pc}, is 648 K. Notably, the experimental wall temperature has surpassed this critical threshold, which in turn poses considerable challenges to the prediction accuracy of ML models.

Fig. 10 provides a detailed breakdown of all experimental boundary conditions. Figs. 10(a) and (b) show data for near-critical and far-critical temperature thresholds, respectively, to validate the ML model's prediction accuracy across the trans-critical region. The conventional SST k-ω model fixed Pr_t=0.85 also serves as the reference for comparison. Fig. 10(a) compares the numerical model results with experimental data in Test 1, with a 2 % absolute error bar shown from $x = 0.4$ m to $x = 1.2$ m. The ML-based Pr_t model matches the experimental data accurately, with errors at all points <2 % even under complex trans-critical conditions. However, the prediction error of conventional model far exceeds 2 %, revealing deficiencies in computational accuracy especially near the trans-critical temperature region. The error analysis also shows that the ML-based model significantly outperforms the conventional SST k-ω model, reducing the e_R from 12.1 % to 6.1 % and the e_S from 16.9 % to 8.5 %. The conventional model struggles with complex heat transfer near the pseudo-critical temperature (648 K), while the ML model effectively captures these non-linear behaviors. Fig. 10(b) presents the comparison results in Test 2, with a 5 % absolute error bar of experimental data. When wall temperature significantly exceeds the critical range, the results of ML-based model align closely with experimental data, with all monitoring point errors consistently <5 %. From inlet to outlet, the new model's results progressively converge toward experimental data. In contrast, while the conventional model captures the experimental trend, its errors substantially exceed 5 %. These findings confirm the new model's computational reliability and stability. While both models exhibit increased prediction errors, the conventional SST k-ω model fails with large errors of e_R=32.6 % and e_S=46.0 %. The ML-based model with e_R=12.5 % and e_S=16.4 %, remains more accurate and aligns better with experimental data. The ML-model's robust performance highlights its capability to capture complex non-linear physics and its potential for reliable supercritical flow simulations.

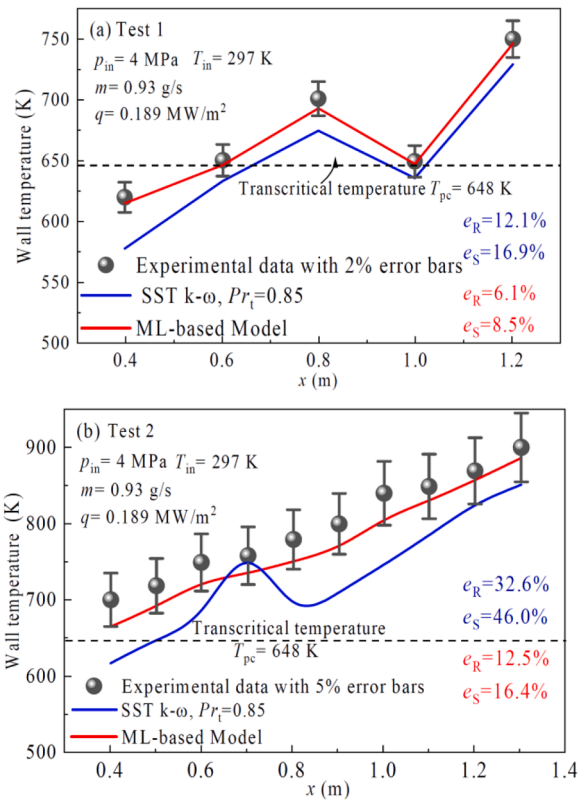


Fig. 10. Comparison of numerical simulation results and experimental data under different mass flow rates and heat fluxes in a horizontal rectangular channel: (a) comparison results with trans-critical temperature characteristics; (b) comparison results above the critical temperature range.

4.4.2. Cross-condition validation: from rectangular to circular channels, and from horizontal to vertical channels

Validation data are sourced from Ref. [52], covering from Test 3 to Test 6. Experimental conditions are summarized in Table 5. The test setup used DC voltage to heat a channel, the inner diameter (d_{in}) of 2.0 mm and length of 759 mm. The mass flow rate is 1.585 g/s with an inlet Reynolds number of 4000, an inlet pressure of 3.0 MPa, and an inlet temperature of 150 °C. The fluid flows vertically upward in Test 3-Test 5, and downward in Test 6. Error bars of 3 %, 5 %, 5 %, and 6 % for Test 1 to Test 4, respectively, are chosen to assess the ML-based model's prediction accuracy.

The evaluation of Tests 3 to 6, with increasing heat flux from 115

Table 4
Experimental condition parameters for heat transfer of hydrocarbon fuel in channel [51].

Test Group	Mass Flow Rate, m (g/s)	Inlet Temperature, T_{in} (K)	Heat Flux, q (kW/m^2)
Test 1	0.93	297	0.189
Test 2	1.24	297	0.341

Table 5
Experimental operating parameters for heat transfer of hydrocarbon fuel in channels [52].

Test group	Flow direction	Mass flow rate, m (g/s)	Inlet temperature, T_{in} (K)	Heat flux, q (kW/m^2)
Test 3	Vertically upward	1.585	423.15	115
Test 4	Vertically upward	1.585	423.15	218
Test 5	Vertically upward	1.585	423.15	306
Test 6	Vertically downward	1.585	423.15	306

kW/m^2 to 306 kW/m^2, shows a widening performance gap between models. Fig. 11(a) compares the numerical model results in Test 3. At low heat flux, experimental wall temperature rises sharply near the x/d_{in}=25 region. The constant-Pr_t model consistently overestimates experimental data from x/d_{in}=25 to x/d_{in}=375. The relative error is 2 % at x/d_{in}=50, increasing to 6.9 % at x/d_{in}=350. This confirms that as x/din increases, the relative error grows dramatically. In contrast, the ML-based Pr_t model has smaller, more stable errors, matching experimental data closely with a maximum error of only 1.7 %. It has always remained within the 3 % error bar range. In Fig. 11(b), at higher heat flux for Test 4, the constant-Pr_t model predicts higher temperatures than experimental data. The errors are small at low x/d_{in} but increased with x/d_{in} to 14.3 %, and these predicted values fall outside the 5 % error bar range. However, the ML-based Pr_t model has smaller, more consistent errors <2.9 %, and captures experimental trends accurately especially in the large x/d_{in} region. In Fig. 11(c), with further increased heat flux to 306 kW/m^2 for Test 5, experimental temperature changes drastically. The constant-Pr_t model deviates significantly from experimental data especially beyond x/d_{in}=200, overestimating temperatures by up to 20 %. The ML-based Pr_t model matches experimental data with a maximum error of 4 % and falls within the 5 % error bar range, which highlights its superior prediction accuracy. In Fig. 11(d), with vertically downward flow for Test 6, experimental temperature rises steadily with x/d_{in}. The constant-Pr_t model also predicts a rising trend but overestimates significantly with a maximum error of 14.29 %. The ML-based Pr_t model aligns closely with experimental results with an error <4.2 %, which indicates its superior accuracy for temperature trend prediction under high heat flux. From the perspective of error metrics, In Test 3, the ML model outperformed the conventional SST k-ω model, with an e_R=3.2 % versus e_R=7.4 %, and an e_S=4.9 % versus e_S=18.9 %. As heat flux increased, the conventional model's errors surged to nearly 50 % in Test 4 and up to 68.7 % in later tests, while the ML model maintained low error rates. This highlights the ML model's superior capability in handling complex, non-linear supercritical flows, making it vital for accurate high-heat-flux simulations.

In summary, as the heat flux increases, the conventional constant-Pr_t model faces significant accuracy challenges. A universal limitation of such models is their inherent assumption of a linear turbulent momentum-thermal transport relationship—rooted fundamentally in using a constant Pr_t. ML offers key advantages for Pr_t model development, which captures nonlinear, complex relationships in turbulent flows and learns these from large datasets. Unlike fixed or empirical coefficients, ML-based models dynamically adjust Pr_t values across grid points based on local flow. Moreover, trained on diverse datasets, ML-based models generalize to new flow scenarios—accelerating the development of reliable, versatile Pr_t models for high-accuracy simulations.

5. Conclusions

SCFs have become indispensable in advanced energy and power systems owing to their unique thermophysical properties. However, accurately modeling their flow and heat transfer behaviours remains a

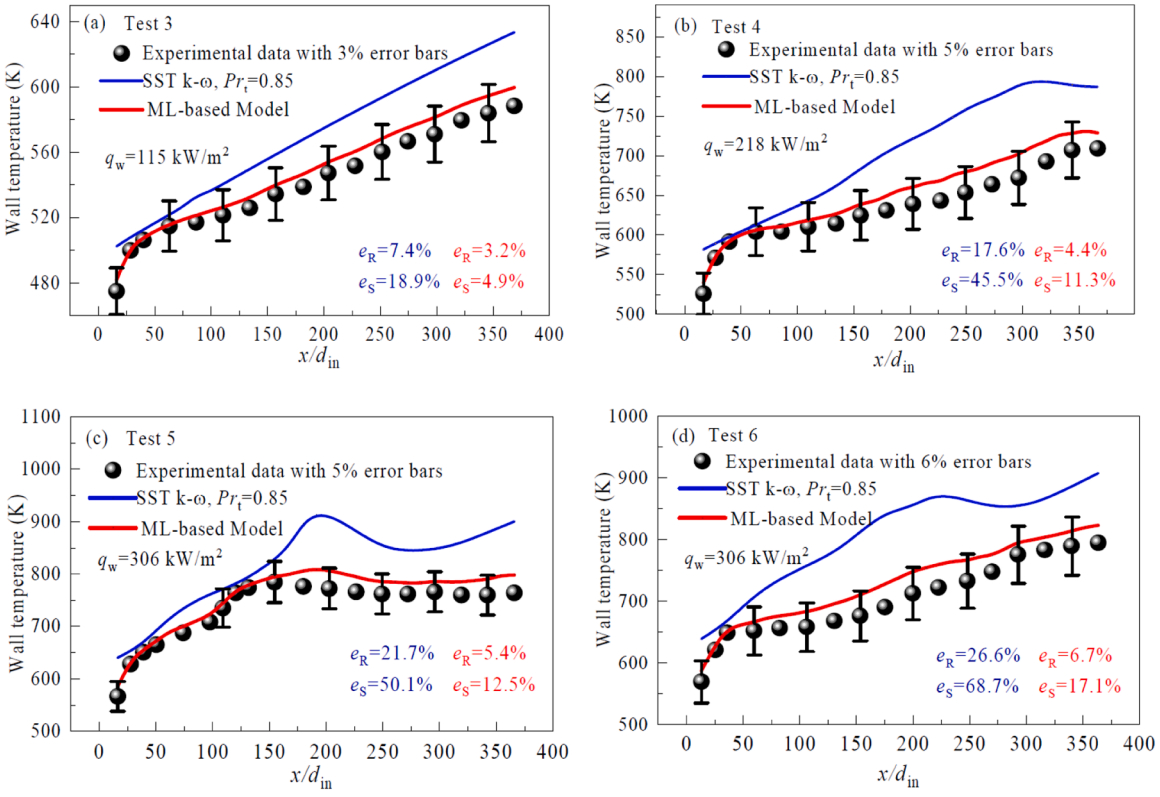


Fig. 11. Comparison of numerical simulation results and experimental data under different heat fluxes in a circular channel: (a)–(c) for vertical upward flow; (d) for vertical downward flow.

critical challenge. It stems from the assumptions of constant Pr_t and isotropic eddy viscosity. This paper proposes a new ML-driven inverse adjoint framework to enable dynamic spatial Pr_t, and enhance the predictive accuracy of RANS models under supercritical pressure. The key conclusions are as follows.

Firstly, this study identifies the main flaw of conventional RANS models. The constant-Pr_t assumption disrupts the link between turbulent heat and momentum transport in SCFs. To address this, high-fidelity LES data serve as a benchmark. The discrete adjoint optimization is employed for Pr_t inversion, and a hybrid RBF-MLP neural network is developed to map nonlinear flow features.

Secondly, an adjoint-based inversion is built in SU2 to compute the gradient dJ/dPr_t of a temperature-based objective function across 10^8 grid points. This gradient is critical for establishing an adjoint relationship with the RBF-MLP network, enabling mapping of key flow features to dynamic Pr_t distributions. Tight coupling of high-fidelity LES data, adjoint gradients, and RBF-MLP mapping allows the new model to accurately capture supercritical thermal behaviors.

Finally, the hydrogen fuel flow under high heat flux is used as a case study. The objective function converged stably after 46 iterations. In a non-uniformly heated rectangular channel test dataset, the adjoint-corrected Pr_t model outperforms the constant-Pr_t model in precision accuracy. For Re and Gr_b, the conventional model shows significant deviations from LES data near the wall ($y=-1$), while the adjoint-corrected model closely matches LES trends.

The cross-condition validation in rectangular channels, shows the adjoint-based model's wall temperature predictions within an acceptable range <2 % for Test 1 and <5 % for Test 2. In vertically flowing circular channels, it captures the sharp inlet-wall temperature rise for Test 3. At higher heat fluxes (Test 4 and Test 5), the conventional model prematurely predicts HTD-related temperature peaks, while the adjoint-corrected model aligns better with experimental data.

Overall, the adjoint-based inversion is a key method for improving model accuracy. However, the inversion model's accuracy degrades in regions with scarce high-quality data—mitigable by increasing mapping samples. This work marks a decisive step from the constant Pr_t corrections to a spatially-resolved, full-field inversion of Pr_t for supercritical turbulent flows. This work provides a robust computational framework, advances understanding of supercritical thermal transport, and establishes adjoint-driven inversion as essential for next-generation, data-informed turbulence models.

CRediT authorship contribution statement

Feng Sun: Writing – original draft, Software, Methodology, Investigation, Funding acquisition, Formal analysis. **Bo Zhang:** Software. **Jinkun Yan:** Validation. **Gongnan Xie:** Writing – review & editing, Supervision. **Jinliang Xu:** Writing – review & editing, Supervision.

Declaration of competing interest

The authors declare that they have no known competing financial interests or personal relationships that could have appeared to influence the work reported in this paper.

Acknowledgements

This work was sponsored by the Natural Science Foundation of China (Youth Program) under Grant No. 52506082, the Scientific Research Fund of Central Universities under Grant No. JB2025020, and the High-Level Talent Introduction Program under Grant No. 219/X9998601.

Appendix. Governing Equations in SU2 Simulations

This appendix outlines the governing equations for the fluid flow and heat transfer simulations performed with the SU2 solver.

A.1. Reynolds-averaged Navier-Stokes (RANS) equations

The core RANS equations for compressible flow solved by SU2 are based on the Favre (density-weighted) averaging. The conservation form of the equations is:

Conservation of Mass:

$$\frac{\partial \overline{\rho}}{\partial t} + \frac{\partial}{\partial x_j}\left(\overline{\rho}\widetilde{u}_j\right) = 0 \tag{A1}$$

Conservation of Momentum:

$$\frac{\partial}{\partial t}\left(\overline{\rho}\widetilde{u}_i\right) + \frac{\partial}{\partial x_j}\left(\overline{\rho}\widetilde{u}_i\widetilde{u}_j\right) = -\frac{\partial \overline{p}}{\partial x_i} + \frac{\partial}{\partial x_j}\left(\overline{\tau}_{ij} - \overline{\rho}\widetilde{u''_i u''_j}\right) \tag{A2}$$

where $\overline{\tau}_{ij}$ is the molecular viscous stress tensor and $-\overline{\rho}\widetilde{u''_i u''_j}$ is the Reynolds stress tensor.

Conservation of Energy:

$$\frac{\partial}{\partial t}\left(\overline{\rho}\widetilde{E}\right) + \frac{\partial}{\partial x_j}\left(\overline{\rho}\widetilde{H}\widetilde{u}_j\right) = \frac{\partial}{\partial x_j}\left(\widetilde{u}_i\overline{\tau}_{ij} + \overline{q}_j - \overline{\rho}\widetilde{u''_j H''}\right) \tag{A3}$$

where $\widetilde{E}$ is the total energy, $\widetilde{H}$ is the total enthalpy, $\overline{q}_j$ is the molecular heat flux, and $-\overline{\rho}\widetilde{u''_j H''}$ is the turbulent heat flux.

The Reynolds stresses are closed using the Boussinesq hypothesis:

$$-\overline{\rho}\widetilde{u''_i u''_j} = \mu_t\left(2\widetilde{S}_{ij} - \frac{2}{3}\frac{\partial \widetilde{u}_k}{\partial x_k}\delta_{ij}\right) - \frac{2}{3}\overline{\rho}k\delta_{ij} \tag{A4}$$

where μ_t is the turbulent eddy viscosity, $\widetilde{S}_{ij}$ is the Favre-averaged strain rate tensor, and k is the turbulent kinetic energy.

The turbulent heat flux is modeled as:

$$-\overline{\rho}\widetilde{u''_j H''} = \frac{\mu_t}{Pr_t}\frac{\partial \widetilde{h}}{\partial x_j} \tag{A5}$$

where Pr_t is the turbulent Prandtl number, the primary focus of the model in this work.

The **Menter's Shear Stress Transport (SST) k-ω model** is used to compute the eddy viscosity.

A.2. Large eddy simulation (LES) governing equations

The LES methodology solves the spatially filtered Navier-Stokes equations. The governing equations are the Favre-filtered conservation laws.

Filtered Conservation of Mass:

$$\frac{\partial \overline{\rho}}{\partial t} + \frac{\partial}{\partial x_j}\left(\overline{\rho}\widetilde{u}_j\right) = 0 \tag{A6}$$

Filtered Conservation of Momentum:

$$\frac{\partial}{\partial t}\left(\overline{\rho}\widetilde{u}_i\right) + \frac{\partial}{\partial x_j}\left(\overline{\rho}\widetilde{u}_i\widetilde{u}_j\right) = -\frac{\partial \overline{p}}{\partial x_i} + \frac{\partial}{\partial x_j}\left(\overline{\tau}_{ij} - \overline{\rho}\left(\widetilde{u_i u_j} - \widetilde{u}_i\widetilde{u}_j\right)\right) \tag{A7}$$

The term $\tau_{ij}^{sgs} = \overline{\rho}\left(\widetilde{u_i u_j} - \widetilde{u}_i\widetilde{u}_j\right)$ is the Subgrid-Scale (SGS) stress tensor, representing the effect of unresolved small scales on the resolved field.

Filtered Conservation of Energy:

$$\frac{\partial}{\partial t}\left(\overline{\rho}\widetilde{E}\right) + \frac{\partial}{\partial x_j}\left(\overline{\rho}\widetilde{H}\widetilde{u}_j\right) = \frac{\partial}{\partial x_j}\left(\widetilde{u}_i\overline{\tau}_{ij} + \overline{q}_j - \overline{\rho}\left(\widetilde{u_j H} - \widetilde{u}_j\widetilde{H}\right)\right) \tag{A8}$$

The term $Q_j^{sgs} = \overline{\rho}\left(\widetilde{u_j H} - \widetilde{u}_j\widetilde{H}\right)$ is the SGS heat flux.

The **Wall-Adapting Local Eddy-Viscosity (WALE) model** is employed to model the SGS stresses. In this model, the SGS stress tensor is modeled as:

$$\tau_{ij}^{sgs} - \frac{1}{3}\tau_{kk}^{sgs}\delta_{ij} = -2\mu_{sgs}\widetilde{S}_{ij} \tag{A9}$$

The subgrid-scale eddy viscosity μ_{sgs} is given by:

$$\mu_{sgs} = \overline{\rho}(C_w\Delta)^2\frac{\left(S_{ij}^d S_{ij}^d\right)^{3/2}}{\left(\widetilde{S}_{ij}\widetilde{S}_{ij}\right)^{5/2} + \left(S_{ij}^d S_{ij}^d\right)^{5/4}} \tag{A10}$$

where C_w is the WALE model constant (typically 0.325), Δ is the filter width, and S_{ij}^d is the traceless symmetric part of the square of the velocity gradient tensor.

Data availability

Data will be made available on request.

References

[1] Z. Hou, C. Yang, H. Wang, H. Li, Heat transfer characteristics and optimization strategies in supercritical fluid heat exchangers with non-uniform thermal boundaries: a systematic review, Int. J. Heat Fluid Flow 110 (2024) 109582.

[2] G.N. Xie, X.X. Xu, X.L. Lei, Z.H. Li, Y. Li, B. Sunden, Heat transfer behaviors of some supercritical fluids: a review, Chin. J. Aeronaut. 35 (1) (2022) 290–306.

[3] X. Xu, L. Teng, W. Ran, Y. Wang, C. Liu, A review of heat transfer deterioration mechanisms and mitigation strategies of supercritical CO_2 heat transfer, Int. J. Heat Fluid Flow 109 (2024) 109534.

[4] F. Sun, G.N. Xie, Turbulence statistics of thermo-buoyancy supercritical fuel flow in a regenerative cooling channel, J. Therm. Sci. 33 (1) (2024) 126–137.

[5] J.H. Park, M.H. Kim, Experimental investigation on comprehensive thermal-hydraulic performance of supercritical CO_2 in a NACA 0020 airfoil fin printed circuit heat exchanger, Int. J. Heat. Mass Transf. 220 (2024) 124947.

[6] J. Huang, Y. Zhou, Y. Huang, Q. Luo, Y. Yuan, C. Yang, W. Hu, Experimental study of pressure drop oscillation in a supercritical carbon dioxide natural circulation loop, Int. J. Heat. Mass Transf. 220 (2024) 125005.

[7] K.T. Lau, S. Ahmad, C.K. Cheng, S.A. Khan, C.M. Eze, J. Zhao, Review on supercritical fluids heat transfer correlations, part I: variants of fundamental dimensionless variables, Heat Transf. Eng. 45 (6) (2024) 552–568.

[8] K.T. Lau, S. Ahmad, C.K. Cheng, S.A. Khan, C.M. Eze, J. Zhao, Review on supercritical fluids heat transfer Correlations, part II: variants of correction factors and buoyancy-related dimensionless variables, Heat Transf. Eng. 45 (6) (2024) 569–583.

[9] B.Q. Yuan, W. Wang, W.J. Du, Assessment of advanced RANS models to predict the heat transfer for supercritical fluids in vertical tubes, Int. J. Heat. Mass Transf. 219 (2024) 124829.

[10] B. Yu, Y. Wang, Q. Liu, W. Shi, J. Xu, Effects of turbulent Prandtl number on supercritical carbon dioxide turbulent flow with high heat flux in vertical round tube, Appl. Therm. Eng. 249 (2024) 123310.

[11] Z. Hou, X. Guo, Z. Liang, K. Yang, C. Yang, H. Wang, Improvement on numerical simulation of supercritical water flow in horizontal tubes: a buoyancy-tuned turbulent Prandtl number model, Int. J. Heat. Mass Transf. 232 (2024) 125928.

[12] P.X. Jiang, Z.C. Wang, R.J. Niu, A modified buoyancy effect correction method on turbulent convection heat transfer of supercritical pressure fluid based on RANS model, Int. J. Heat. Mass Transf. 127 (2018) 257–267.

[13] A. Piccinelli, W. Ambrosini, W. Andreini, Prediction of heat transfer to supercritical fluids by the use of algebraic heat flux models, Nucl. Eng. Des. 297 (2016) 257–266.

[14] A. Piccinelli, W. Ambrosini, Improvements in the prediction of heat transfer to supercritical pressure fluids by the use of algebraic heat flux models, Ann. Nucl. Energy 99 (2017) 58–67.

[15] R. Zhang, Z. Yang, Y. Liu, Q. Qiu, X. Zhu, An interpretable machine learning-based model of turbulent prandtl number for supercritical CO_2 under buoyancy, Appl. Therm. Eng. 6 (2025) 126744.

[16] T. Murugan, A. Agrawal, S.K. Saha, Proposal of a turbulent Prandtl number model for predicting heat transfer deterioration in supercritical flows, Phys. Fluids 37 (9) (2025) 095115.

[17] C.R. Zhao, Z. Zhang, P.X. Jiang, H.L. Bo, Influence of various aspects of low Reynolds number k-ε turbulence models on prediction of in-tube buoyancy affected heat transfer to supercritical pressure fluids, Nucl. Eng. Des. 313 (2017) 401–413.

[18] M. Mohebbi, M. Bazargan, Effect of turbulent Prandtl number on convective heat transfer in turbulent flows of a supercritical fluid in a vertical round tube, J Heat Transf. 130 (2008) 022501.

[19] J. Liu, Y. Jin, P. Zhao, Z. Ge, Y. Li, Y. Wan, Analysis of heat transfer of supercritical water by direct numerical simulation of heated upward pipe flows, Int. J. Therm. Sci. 138 (2019) 206–218.

[20] Y.Y. Bae, A new formulation of variable turbulent prandtl number for heat transfer to supercritical fluids, Int. J. Heat. Mass Transf. 92 (2016) 792–806.

[21] M. Bazargan, M. Mohseni, The significance of the buffer zone of boundary layer on convective heat transfer to a vertical turbulent flow of a supercritical fluid, J. Supercrit. Fluids 51 (2) (2009) 221–229.

[22] M. Duponcheel, L. Bricteux, L. Manconi, M. Winckelmans, G. Bartosiewicz, Assessment of RANS and improved near-wall modeling for forced convection at low prandtl numbers based on LES up to re-τ= 2000, Int. J. Heat. Mass Transf. 75 (2014) 470–482.
[23] H. Kawamura, K. Ohsaka, H. Abe, K. Yamamoto, DNS of turbulent heat transfer in channel flow with low to medium-high Prandtl number fluid, Int. J. Heat Fluid Flow 19 (5) (1998) 482–491.
[24] M. Mohseni, M. Bazargan, Effect of turbulent Prandtl number on convective heat transfer to turbulent flow of a supercritical fluid in a vertical round tube, J. Heat Transf.-Trans. ASME 133 (7) (2011) 071701.
[25] J. Howell, S. Lee, Convective heat transfer in the entrance region of a vertical tube for water near the thermodynamic critical point, Int. J. Heat. Mass Transf. 42 (7) (1999) 1177–1187.
[26] S. Lee, J. Howell, Turbulent developing convective heat transfer in a tube for fluids near the critical point, Int. J. Heat. Mass Transf. 41 (10) (1998) 1205–1218.
[27] Manda, U., Mazumdar, S. Effects of buoyancy in a horizontal microchannel in a laminar flow of supercritical carbon dioxide (SCO2) at different gravities [R]. Available at SSRN 4591011, 2023.
[28] Manda, U., Mazumdar, S. Effect of cross-sectional shape on flow and heat transfer characteristics of the laminar flow of supercritical carbon dioxide (SCO2) inside horizontal microchannels. Available at SSRN 4596518, 2023.
[29] G. Tang, H. Shi, Y. Wu, J. Lu, Z. Li, Q. Liu, H. Zhang, A variable turbulent Prandtl number model for simulating supercritical pressure CO_2 heat transfer, Int. J. Heat. Mass Transf. 102 (2016) 1082–1092.
[30] X. Du, Z. Lv, X. Yu, M. Cao, J. Zhou, Y. Ren, Q. Qiu, X. Zhu, Heat transfer of supercritical CO_2 in vertical round tube: a considerate turbulent prandtl number modification, Energy 192 (2020) 116612.
[31] F. Sun, G.N. Xie, J. Song, C.N. Markides, Proper orthogonal decomposition and physical field reconstruction with artificial neural networks (ANN) for supercritical flow problems, Eng. Anal. Bound. Elem. 140 (2022) 282–299.
[32] C.D. Ellis, H. Xia, G.J. Page, LES informed data-driven modelling of a spatially varying turbulent diffusivity coefficient in film cooling flows[C]//Turbo Expo: power for Land, Sea, and air, Am. Soc. Mech. Eng. 84171 (2020). V07BT12A029.
[33] R.D. Sandberg, R. Tan, J. Weatheritt, A. Ooi, A. Haghiri, V. Michelassi, G. Laskowski, Applying machine learnt explicit algebraic stress and scalar flux models to a fundamental trailing edge slot, J. Turbomach. 140 (10) (2018) 101008.
[34] P.M. Milani, J. Ling, G. Saez-Mischlich, J. Bodart, J.K. Eaton, A machine learning approach for determining the turbulent diffusivity in film cooling flows, J. Turbomach. 140 (2) (2018) 021006.
[35] C.D. Ellis, H. Xia, Vector-based neural network turbulent heat flux closures in near-wall cooling jet flows, Int. J. Heat. Mass Transf. 244 (2025) 126893.
[36] J. Ling, J. Templeton, Evaluation of machine learning algorithms for prediction of regions of high Reynolds averaged Navier Stokes uncertainty, Phys. Fluids 27 (8) (2015) 085103.
[37] E.J. Parish, K. Duraisamy, A paradigm for data-driven predictive modeling using field inversion and machine learning, J. Comput. Phys. 305 (2016) 758–774.
[38] J.R. Holland, J.D. Baeder, K. Duraisamy, Towards integrated field inversion and machine learning with embedded neural networks for RANS modeling, InAIAA Scitech 2019 forum (2019) 1884.
[39] Z. Zhang, Y.B. Mao, X.R. Su, X. Yuan, Inversion learning of turbulent thermal diffusion for film cooling, Phys. Fluids 34 (3) (2022) 035118.
[40] E.J. Parish, K. Duraisamy, A paradigm for data-driven predictive modeling using field inversion and machine learning, J. Comput. Phys. 305 (2016) 758–774.
[41] A.P. Singh, S. Medida, K. Duraisamy, Machine-learning-augmented predictive modeling of turbulent separated flows over airfoils, AIAA J. 55 (7) (2017) 2215–2227.
[42] X.L. Zhang, H. Xiao, X.D. Luo, G. He, Ensemble Kalman method for learning turbulence models from indirect observation data, J. Fluid. Mech. 949 (2022) A26.
[43] Z.Y. Wang, W.W. Zhang, A unified method of data assimilation and turbulence modeling for separated flows at high reynolds numbers, Phys. Fluids 35 (2) (2023) 025124.
[44] K.J. Ryan, J. Bodart, M. Folkersma, C.J. Elkins, J.K. Eaton, Turbulent scalar mixing in a skewed jet in crossflow: experiments and modeling, Flow Turbul. Combust. 98 (3) (2017) 781–801.
[45] N. Fonzi, S.L. Brunton, U. Fasel, Data-driven modeling for transonic aeroelastic analysis, J. Aircr. 61 (2) (2024) 625–637.
[46] P. Yan, G. Gori, M. Zocca, A. Guardone, SU2-COOL: open-source framework for non-ideal compressible fluid dynamics, Comput. Phys. Commun. 307 (2025) 109394.
[47] F. Sun, G.N. Xie, J. Song, C.N. Markides, Thermal characteristics of in-tube upward supercritical CO_2 flows and a new heat transfer prediction model based on artificial neural networks (ANN), Appl. Therm. Eng. 194 (2021) 117067.
[48] F. Sun, Y. Li, O. Manca, G.N. Xie, An evaluation on the laminar effect of buoyancy-driven supercritical hydrocarbon fuel flow and heat transfer characteristics, Int. J. Heat. Mass Transf. 142 (2019) 118414.
[49] Y. Chen, Y. Li, B. Sunden, G.N. Xie, The abnormal heat transfer behavior of supercritical n-decane flowing in a horizontal tube under regenerative cooling for scramjet engines, Appl. Therm. Eng. 167 (2020) 114637.
[50] B.H. Yu, Y.J. Wang, Q.B. Liu, W.J. Shi, J.L. Xu, Effects of turbulent Prandtl number on supercritical carbon dioxide turbulent flow with high heat flux in vertical round tube, Appl. Therm. Eng. 249 (2024) 123310.
[51] L. Zhang, J.L. Le, R.L. Zhang, X.W. Zhang, K. Jing, Heat transfer of hydrocarbon fuel in turbulent flow region under supercritical pressure, J. Propuls. Technol. 34 (2013) 225–229.
[52] B. Liu, Y.H. Zhu, J.J. Yan, Y.T. Lei, B. Zhang, P.X. Jiang, Experimental investigation of convection heat transfer of n-decane at supercritical pressures in small vertical tubes, Int. J. Heat. Mass Transf. 91 (2015) 734–746.